

## Chapter 2

**An InSAR-based survey of deformation in the central Andes, Part II: Modeling the volcanic deformation – sensitivity to source geometry and mass balance in a volcanic arc**

# Abstract

We model four centers of volcanic deformation (observed with radar interferometry) in the central Andes. To explore the range of source depths and volumes allowed by our observations, we use spherical, ellipsoidal and crack-like source geometries. We further examine the effects of local topography upon the deformation field and invert for a spherical point-source in both elastic half-space and layered-space crustal models. We use a global search algorithm, with gradient search methods used to further constrain best-fitting models. Source depths are model-dependent, with differences in the assumed source geometry including a larger range of inferred depths than variations in elastic structure. Source depths relative to sea level are: 8-18 km at Hualca Hualca; 12-25 km for Uturuncu; 5-13 km for Lazufre, and 5-10 km at Cerro Blanco. We observe a region of localized subsidence NE of Hualca Hualca that could be from fumarolic activity or a shallow earthquake, but would require that the catalog locations for this event be off in location and depth by 10-50 km. Deformation at all four volcanoes seems to be time-dependent, and only Uturuncu and Cerro Blanco were deforming during the entire time period of observation. An increased rate of inflation at Uturuncu and Lazufre may be correlated with a  $M_w$  7.1 subduction zone earthquake. Conductive cooling and crystallization of a magma chamber alone can not explain the rate of subsidence at Cerro Blanco, thereby suggesting the existence of a hydrothermal system to increase the cooling rate and/or to cause subsidence through poroelastic effects. For the last decade, the ratio of the volume intruded to extruded magma is about 1-10, which agrees with previous geologic estimates in this and other volcanic arcs. The combined rate of intrusion and extrusion is within an order of magnitude of the inferred geologic rate.

## 2.1 Introduction

Using interferometric synthetic aperture radar (InSAR), we identified four centers of volcanic deformation at remote volcanoes in the central Andes (14-27°S, *Pritchard and Simons, 2002*), see Figure 2.1. We do not know if the deformation is caused by pressurization of a magma chamber that will eventually cause an eruption, or if it is related to more benign ongoing processes of non-eruptive intrusion, crustal melting, or hydrothermal activity. Therefore, it is difficult to assess the threat of a given episode of deformation to local populations or to overflying aircraft. By themselves, observations of deformation cannot be used for hazard assessment at a given remote volcano – historical records of the relationship between eruptions and other observations (including seismic, geochemical, and deformation studies) are needed.

However, observations of deformation can provide some clues to the physical processes involved by constraining the potential volume of magma moving at depth and the location and temporal evolution of the deformation. For example, hydrothermal systems are thought to be shallower than 10 km, so a deeper source of deformation could suggest a magmatic origin. It is less clear if the horizontal position of the source (e.g., location relative to the edifice) is important in assessing the origin or threat of the deformation. While one might assume that a source of deformation at some distance from an eruptive vent might be a non-eruptive intrusion, several eruptions seem to have been fed by magma chambers 5-10 km away from the eruptive center, as discussed more below. The time evolution of the deformation field can provide assistance in hazard assessment – for example, different threat levels might be inferred in areas where deformation is accelerating as opposed to areas where the deformation is slowing down or stopping. The potential size of an eruption can also be crudely assessed by constraining the volume of moving subsurface magma.

Although deformation data can provide useful constraints on source processes, the data are subject to multiple interpretations. Due to the unknown nature of the source of deformation (*i.e.*, source's shape, spatial extent, depth, etc.), and the spatial vari-

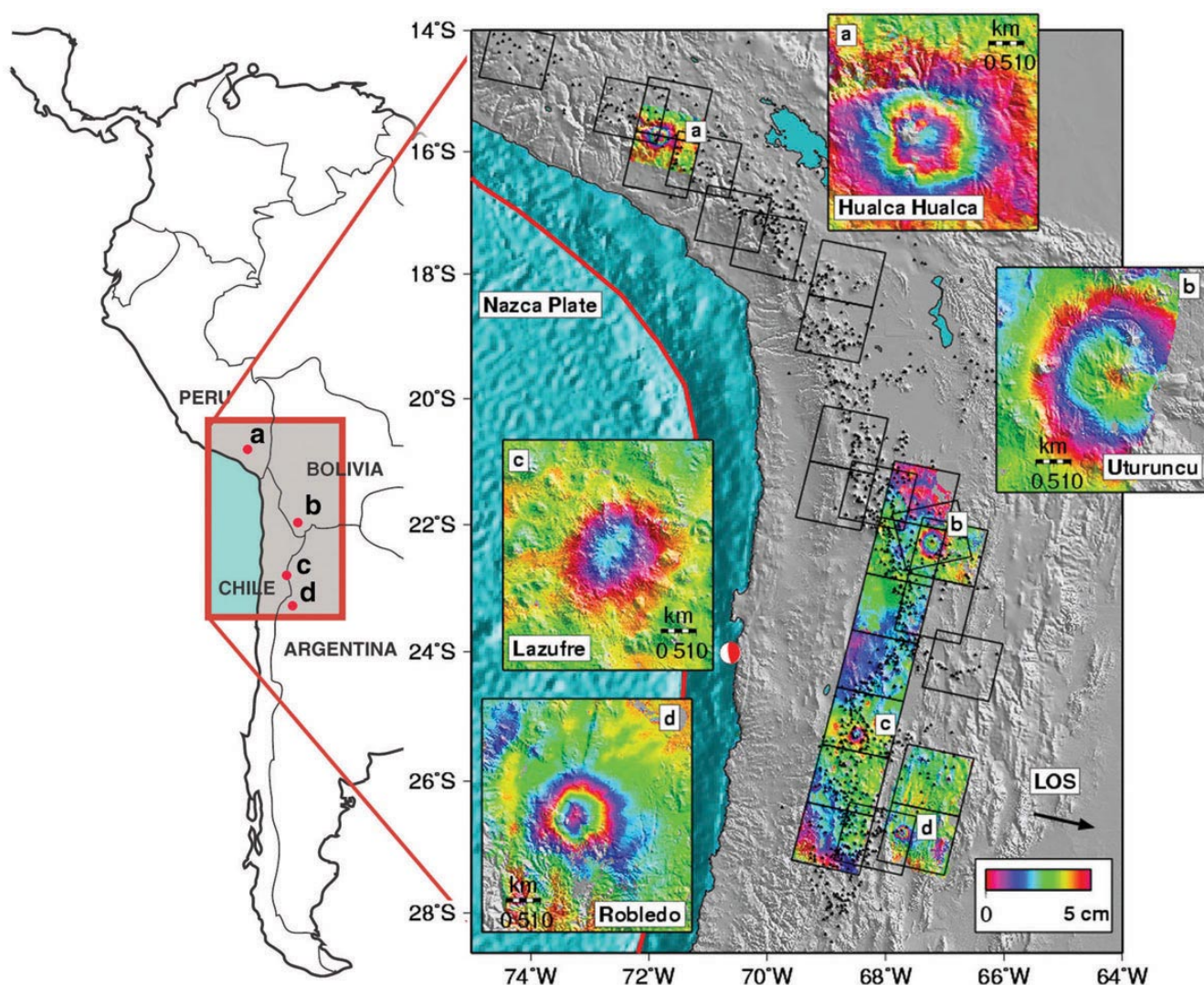


Figure 2.1: Right: Shaded relief topographic map of the central Andes indicating the radar frames used in this study (black squares). Black triangles show the 1,113 potential volcanic edifices (*de Silva and Francis, 1991*). The red line in the ocean is the location of the trench. Color shows interferograms from this study indicating active deformation – each color cycle corresponds to 5 cm of deformation in the radar line-of-sight (LOS) direction. Arrow shows radar LOS direction from ground to spacecraft, which is inclined  $23^\circ$  from the vertical. The red and white earthquake mechanism indicates the location of the  $M_w$  7 subduction zone earthquake mentioned in the text that is temporally correlated with increases in the rates of inflation at Uturuncu and Lazufre. Inset maps provide detailed looks at the centers of volcanic deformation (see Table 2.1 for exact dates): **a**, Hualca Hualca, Peru, time span 6/1992-4/1996 (3.9 yr), **b**, Uturuncu, Bolivia, time span 5/1996-12/2000 (4.6 yr), **c**, Lazufre, time span 5/1996-12/2000 (4.6 yr), all of which are inflating, and **d**, Robledo, time span 5/1996-10/2000 (4.4 yr), in NW Argentina which is deflating. Left: Location of deformation centers within larger South American context. (Reference map created by Doug Cummings, Caltech Public Relations).

ation of the elastic properties of the crust, surface observations provide non-unique constraints on processes occurring at depth. It is most often assumed that the source is a spherically symmetric point source and that the ground is an isotropic, homogeneous half-space (the so-called “Mogi” model), although non-spherical sources, and finite sources have also been explored (*Dieterich and Decker, 1975; Davis, 1986; Yang et al., 1988; Fialko et al., 2001a*). The sources of deformation are usually assumed to be caused by changes in volume (due to the injection or withdrawal of magma or hydrothermal fluids, and/or expansion and contraction caused by temperature or phase changes), such that there is no component of shear. Non-spherical sources that are prolate (“pluton-like”), or oblate (“sill-like”) ellipsoids might be more realistic than a spherical source (e.g., *Davis, 1986*). Yet, the practical limitations that observations are made at the Earth’s surface, and are often limited to a single component of deformation, mean that it is difficult to differentiate between the types of sources (*Dieterich and Decker, 1975; Fialko et al., 2001a*). For example, while it is possible to use multiple InSAR observations from many different viewing geometries to construct a complete 3-D deformation field (*Fialko et al., 2001b*), in the central Andes, data is frequently only available from a single satellite line-of-sight (LOS) direction. In fact, only two interferograms were made from ascending data in our analysis. Conversely, when more than one component of deformation is available, better constraints can be made upon the source geometry (*Dieterich and Decker, 1975; Fialko et al., 2001b*).

When only one component of InSAR data is available, the data can be fit equally well fit by multiple types of sources. For a given deformation source, the different source geometries have different inferred depths. A prolate source with the largest axis vertical gives shallower depths than an oblate source (*Fialko et al., 2001b*). There is also a trade-off between source depth and source strength (or the volume of magma injection/withdrawal), such that to get roughly equivalent surface deformation a deeper source requires a larger source strength. A further complication is that if the elastic medium is not a half-space, but is a more realistic layered and heterogeneous structure, the source depth can be effected (e.g., *Du et al., 1997; Cattin et al., 1999*). Inferred source depths can also be impacted by including the effects of topography

instead of simply assuming a half-space (e.g., *Williams and Wadge, 1998*).

Considering all of the variables, the primary purpose of this chapter is to explore a range of models that fit the data, with different elastic structures and source geometries, both including topography or neglecting it. We then use these modeling results to discuss the time evolution of the deformation, the possible physical sources of the deformation, and estimate the overall rate of intrusion and extrusion in the central Andes during the time period. In the previous chapter, we document the technique and data used in the survey, the sensitivity of our measurements, and the observations of volcanic and non-volcanic deformation.

## 2.2 Modeling strategy

Given an elastic structure (half-space or layered-space) and a deformation source type (spherical, axisymmetric prolate or oblate spheroids), we minimize the misfit between data and model in a least-squares sense ( $L_2$  norm). For problems (like ours) that are non-linear with noisy data, there may be many local minima in the misfit surface (e.g., *Cervelli et al., 2001*). An inversion method must reveal the range of models that fit the data. We use the Neighbourhood Algorithm (NA, *Sambridge, 1998, 1999a,b, 2001*), which samples the entire model parameter space, but focuses on regions of low misfit. The NA method seems able to find many local minima with only two user supplied tuning parameters, and has been used in several geophysical applications (e.g., *Sambridge and Kennett, 2001; Lohman et al., 2002*). We use the NA to generate scatter plots that show misfit as a function of the various model parameters to determine whether an individual parameter is well constrained, and determine the correlation between pairs of variables. In tests with synthetic noisy data, we were able to solve for the input variables with the NA algorithm when there were few model parameters (e.g., the spherical point source). However, when the number of model parameters is increased, (e.g., the prolate ellipsoid) there were so many nearly equal minima in misfit space that the algorithm did not always recover the input parameters. Therefore, in order to more fully explore parameter space, we have also

done inversions using conjugate gradient methods (Gauss-Newton and Levenberg-Marquardt, as implemented in the MATLAB Optimization Toolbox). These methods are more susceptible to local minima, so we have used a variety of initial conditions (sometimes motivated by results from the NA algorithm) to better understand the range of acceptable model parameters. For example, because we are interested in the range of source depths that can explain the deformation, we start the prolate ellipsoid model at a variety of source dips and depths and the penny-shape crack with many different depths and radii. In the results discussed below, we use both complementary methods to constrain the range of source depths.

Because of the non-uniqueness of inverting one component of deformation for source characteristics mentioned above, we choose to invert for as few parameters as possible. Before we begin the inversion, we mask out the region of volcanic deformation, then estimate the best-fitting 2-D linear ramp with three variables (or in rare cases, a quadratic ramp with six components) that removes the long-wavelength signals caused by orbital errors, atmospheric effects, or broad deformation unrelated to the local volcano. In particular, we have found that quadratic changes in the baseline become important when many image frames (as many as seven in this study) are concatenated together (*Pritchard et al., 2002*), and so for those scenes we estimate the quadratic baseline variation during processing. Even after removing the ramp, we allow the inversion to solve for an absolute (constant) offset between the InSAR measurements and the model prediction, because InSAR measures only relative, not absolute displacement.

For all sources, we invert for the  $x$ ,  $y$ , and  $z$  location of the source, and the absolute offset. For the spherically symmetric source we also estimate the volume injected/withdrawn. For the prolate ellipsoid (*Yang et al., 1988*), we fix the semi-major axis to be 1 km (which effectively makes the ellipsoid a point source), because the effects of the finite size of the source are only important in extreme and probably unrealistic conditions involving an extremely large source that extends near the surface. Furthermore, our tests with synthetic and real data indicate that the InSAR observations are rather insensitive to the finite size for our deformation sources (e.g.,

there is a trade-off between source radius, source depth and source volume), which are more than a few km deep. In addition to the parameters mentioned above, for the prolate ellipsoid we also solve for the pressure change, ratio between the semi-major and semi-minor axes, and the strike and dip of the ellipsoid. For the penny-shaped crack (*Fialko et al.*, 2001a), we solve for the radius of the crack and the pressure change. For each volcano, we jointly invert as much data from different time periods or satellite tracks – each of which has a slightly different viewing geometry – as possible. The unwrapped data used in the inversion has been spatially averaged to yield a pixel resolution of about 350 m, sufficient to resolve the smooth deformation pattern from deep magma sources. The data is resampled based on the local curvature of the deformation field (*Simons et al.*, 2002) such that typically several thousand points are used in any inversion (a few percent of the original number of pixels). In the joint inversions, we solve for a single location and source geometry for all interferograms, but allow the source strength to be solved independently for each time span.

For the spherical point source, we generate surface displacements in a half-space and layered-space using propagator matrices with frequency-wavenumber (F-K) summation via the Elementary Displacement Kernel (EDK) software (*Simons and Rivera*, in preparation, 2003). For a given elastic structure, we pre-calculate displacement kernels for “elementary” point sources. Surface deformation from an arbitrary point source can be quickly calculated by a linear combination of the “elementary” cases. This method puts most of the time-intensive computation up front, allowing for fast calculation of displacement given changing source characteristics.

The crust of the central Andes is both laterally and vertically variable, and although there have been many recent investigations of velocity structure (e.g., *Wigger et al.*, 1994; *Yuan et al.*, 2000), the exact structure in the vicinity of each deforming edifice is poorly constrained. A particular complication is the variable existence, depth, and magnitude of low velocity zones throughout the region that have been used to infer zones of partial melting (e.g., *Schmitz et al.*, 1997; *Chmielowski et al.*, 1999; *Yuan et al.*, 2000). Considering the uncertainties, we have chosen to test the effects on the inferred source depth from three different 1-D layered elastic models

for the spherical point source, in addition to the elastic half-space. To use the EDK program, we specify the P-wave velocity,  $V_p$ , the S-wave velocity,  $V_s$ , and the density. We take the  $V_p$  for our models from different locations in the western cordillera and Altiplano from the seismic profile of *Wigger et al.* (1994) at 21°S (Figure 2.2). We use the density values along the same profile from *Schmitz et al.* (1997) that have been constrained by gravity. *Schmitz et al.* (1997) found that standard relations between velocity and density did not match the gravity in some locations, possibly due to the presence of partial melt, and so modified the density in those regions to match the gravity. We assume that the elastic structure is Poissonian, although there are indications that  $V_p/V_s$  is not Poissonian (by about 4%) in the crust beneath at least parts of the volcanic arc (*Myers et al.*, 1998; *Graeber and Asch*, 1999). However, the exact spatial distribution of these variations is not well constrained. Although the velocity models we use are motivated by data, we do not believe the details – since they are sensitive to the chosen parameterization. The models were chosen mostly to represent some end-member velocity structures, and as we show below, the results are not very sensitive to the exact structure chosen.

We explore the sensitivity of surface deformation to two elastic structures (Figure 2.2). Model L1 has two low-velocity zones (LVZ), between 10-20 km and below 25 km, and model L2 only has the LVZ below 25 km. The LVZ below about 25 km is a pervasive feature in the central Andes, although its depth is variable (*Yuan et al.*, 2000), while the shallower LVZ is more spatially variable (*Wigger et al.*, 1994). The velocity and density are extremely variable in the uppermost layer, although our tests indicate that for the source depths in the regions considered, the inferred source depth is not very sensitive to reasonable variations in those parameters. The relative amplitude of surface deformation from the half-space and layered models is sensitive to the depth of a given source. For example, it is well known that weak upper layers amplify the deformation from a given source, and so layered models which have a lower rigidity uppermost layer understandably have more deformation than the half-space for a shallow source (< 3 km). However, as the source depth becomes greater, one must integrate the difference in rigidity between the source and the surface in the models

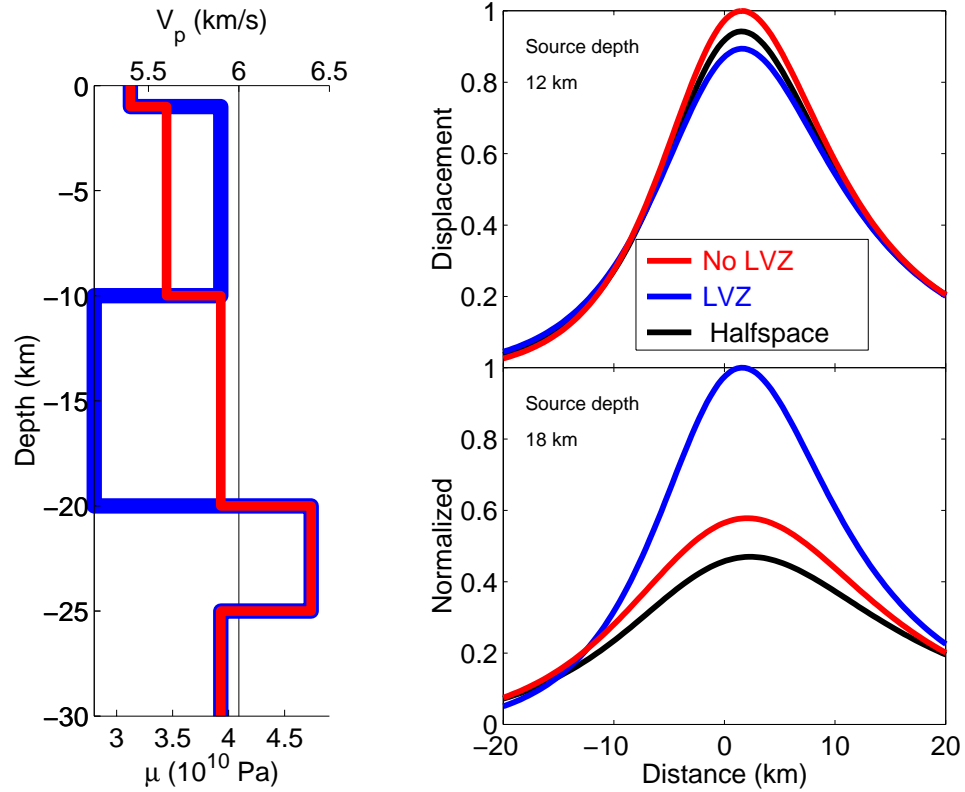


Figure 2.2: The effects of different elastic structures on surface deformation. (Left) Velocity as a function of depth used for the half-space and two layered-space models considered. (Top right) Surface deformation (normalized by the maximum displacement of the three models) in the radar LOS for the three elastic media with a constant source at 12 km. (Bottom right) Surface deformation in the radar LOS for the three elastic media with a constant source at 18 km. See text for details.

to be able to predict the relative amplitudes of surface deformation. The right panels of Figure 2.2 show an example of this effect. In the top right panel, the source is located at 12 km, and the weak upper layers of the L2 structure allow deformation to exceed that from the half-space, while the location of the source within the upper LVZ of L1, reduces the deformation compared to that of the half-space. When the source is moved deeper, to 18 km, deformation from model L2 still exceeds deformation in the half-space. In addition, the integrated effect of the LVZ in model L1 allows deformation to surpass that of the half-space. Thus, the presence and depth extent of the LVZs can influence deformation. However, in the next section, we show that for our sources, the variable material properties seem to have only a secondary impact on inferred source depth compared to different source geometry.

## 2.3 Results

### 2.3.1 Uturuncu

Figure 2.3 shows the data, model, residual and profiles for three interferograms from three different tracks of satellite data. A complete list of the interferograms used in the inversions for this and the other volcanoes is shown in Table 2.1. The observed and predicted interferograms are shown as rates (maximum  $\sim 1\text{-}2$  cm/yr in the radar LOS), while the residual and profiles are shown as absolute displacements. The data shown is cropped from the full interferogram, but we have done other inversions using nearly the complete interferograms, and the results in terms of source depths, location and strengths are similar, although the model fit to the data is not as good.

Using the NA algorithm, we estimate misfit as a function of the different model parameters for three elastic media: half-space, model L1 and model L2 (Figure 2.4). The inversions shown used five interferograms from the three different satellite tracks. Although the misfit function is usually peaked near the best estimate, because of the data noise and non-uniqueness of the problem, we instead choose to use the width of the misfit function to specify a range of values for each parameter. The half-space

Volcano	Track	Frame(s)	Master image	Slave image	$B_{\perp}$ (m)
Hualca Hualca	454	3925	25 Apr. 1996	2 Jun. 1992	60
	454	3915-3933	7 Dec. 1995	7 Jul. 1992	170
	454	3925	31 Jan. 1997	31 Aug. 1993	70
	454	3915-3933	18 Oct. 1996	7 Jul. 1992	80
	454	3925	24 Aug. 1995	31 Aug. 1993	50
	454	3915-3933	2 Oct. 1997	18 Oct. 1996	140
	454	3925	31 Jan. 1997	24 Aug. 1995	120
	454	3915-3933	2 Oct. 1997	7 Jul. 1992	130
	454	3915-3933	13 Sep. 1996	2 Oct. 1997	160
	454	3925	31 Jan. 1997	13 Sep. 1996	130
	454	3915-3933	18 Oct. 1996	7 Dec. 1995	260
	454	3925	13 Sep. 1996	31 Aug. 1993	205
	454	3915-3933	2 Nov. 1995	7 Jul. 1992	270
	454	3915-3933	2 Nov. 1995	21 Dec. 2001	110
	454	3925	24 Aug. 1995	13 Sep. 1996	260
	89	6867	10 Jan. 1999	9 Jul. 2001	170
	p424	327	22 Oct. 1996	12 Apr. 1994	600 <sup>1</sup>
	p424	327	5 Dec. 1996	12 Apr. 1994	150 <sup>1</sup>
	454	3915-3933	7 Dec. 1995	21 Dec. 2001	220
	89	6849	11 Jan. 1999	15 Apr. 2002	120 <sup>2</sup>
454	3915	25 Apr. 1996	5 Apr. 2002	290 <sup>2</sup>	
Uturuncu	3	6741	6 Oct. 1997	4 Apr. 2000	80
	282	4059	18 May 1996	24 Dec. 2000	30
	282	4059	13 Apr. 1996	6 Aug. 2000	60
	282	4059	12 Aug. 1995	24 Dec. 2000	120
	282	4059	12 Aug. 1995	19 May 1996	20
	10	4059	2 May 1992	7 Oct. 1997	100
	10	4059	7 Oct. 1997	21 Dec. 1999	150
	10	4059	2 May 1992	30 Apr. 1996	270
	10	4059	2 Oct. 1995	21 Dec. 1999	20
	10	4059	2 Oct. 1995	7 Oct. 1997	130
	10	4059	2 May 1992	21 Dec. 1999	250
10	4059	2 May 1992	2 Oct. 1995	220	
Lazufre	282	4113	8 Jul. 1995	26 Oct. 1997	65
	282	4113	13 Apr. 1996	8 Aug. 2000	70
	282	4113	14 Apr. 1996	8 Aug. 2000	150
	282	4113	12 Aug. 1995	24 Dec. 2000	180
	282	4113	18 May 1996	24 Dec. 2000	80
	282	4113	19 May 1996	24 Dec. 2000	190
	282	4113	26 Oct. 1997	7 Jul. 2002	120 <sup>2</sup>
	282	4113	12 Aug. 1995	19 May 1996	15
Cerro Blanco	10	4149	30 Apr. 1996	2 May 1992	270
	10	4149	7 Oct. 1997	2 May 1992	170
	239	4149	12 Oct. 2000	16 May 1996	5
	10	4149	2 Oct. 1995	2 May 1992	300
	10	4149	7 Oct. 1997	2 Oct. 1995	130
	10	4149	6 Oct. 1997	2 Oct. 1995	210
	10	4149	29 Apr. 1996	2 May 1992	190

Table 2.1: Interferograms made at the four actively deforming centers and used in the inversions for source parameters. <sup>1</sup>The two JERS interferograms were stacked together to increase the signal-to-noise ratio (see text). <sup>2</sup>These interferograms were attempted, because the ERS catalog indicated that they were on the correct Doppler ambiguity. However, the interferograms could not be made, perhaps indicating a problem with the ERS Doppler catalog.

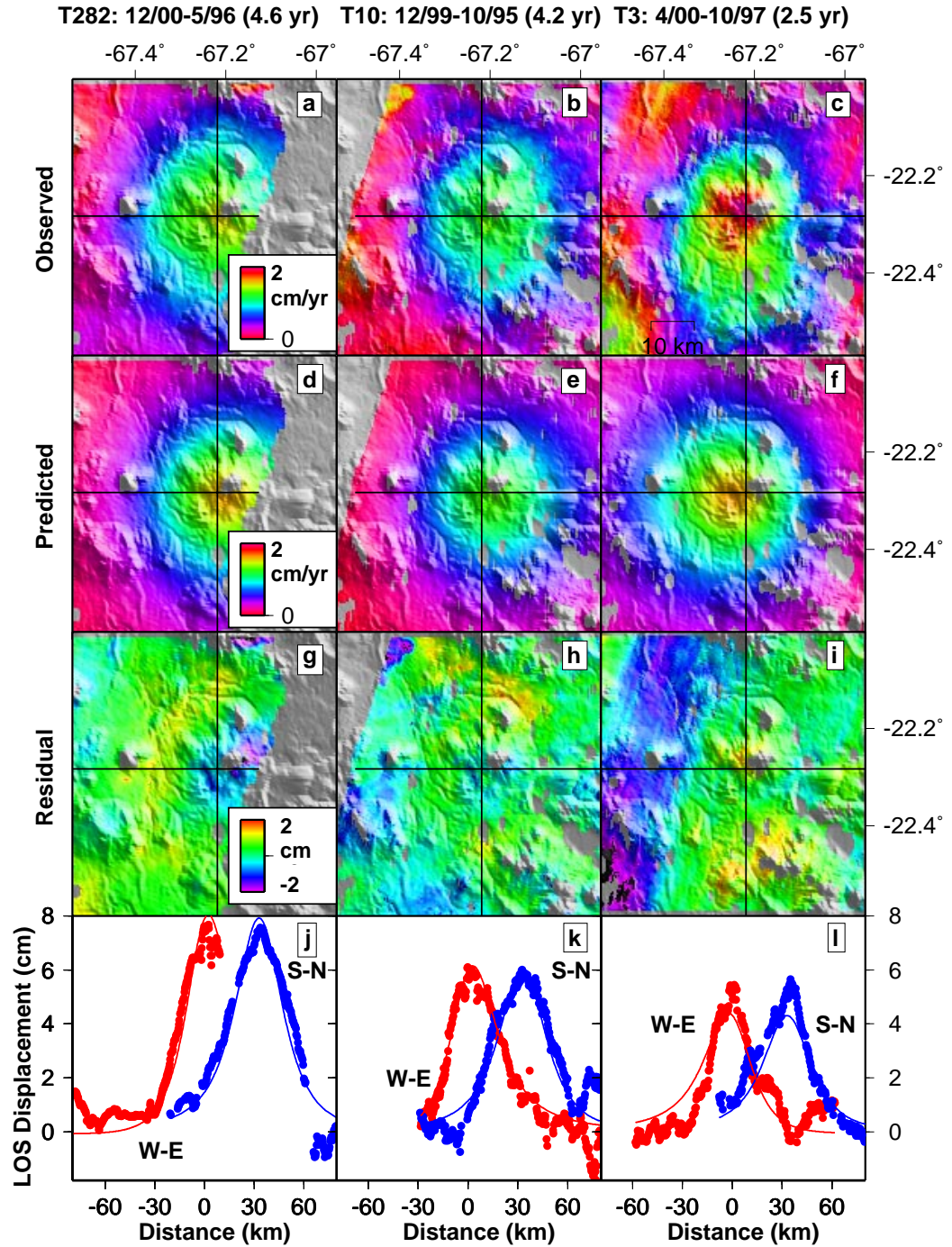


Figure 2.3: Observed (a., b., c.) and modeled rates (d., e., f.) of deformation (cm/yr) at Uturuncu in three independent interferograms, from two different tracks of descending InSAR data and one ascending track. Black lines are the locations of profiles shown in the bottom row of the figure. The black lines run through the inferred center of the deformation source, and may appear offset from the center of the deformation pattern because of the projection of the deformation into the LOS. g., h., i. Residual between data and model, shown as displacement. j., k., l. South-north and west-east profiles through the model and data, where the south-north profile has been offset for the sake of clarity.

model provides the best fit, perhaps because of our crude parameterizations of the layered structure. In the presence of noise, there is a trade-off between source depth and strength (Figure 2.5) – a deep and strong source can look like a shallow weak source. When multiple interferograms (which have different realizations of noise) are used in an inversion, the trade-off for each individual interferogram is slightly reduced because of the additional datasets. For example, inversions done using only single interferograms give different source depths (Figure 2.5), but when the data are combined in a joint inversion, the range in inferred depths is narrower (Figure 2.4). For the level of noise in these interferograms, we find that for resolving source depth and strength at this volcano with data from ERS, it does not seem to matter whether the multiple interferograms are from different orbital tracks (with slightly different viewing geometries) or the same one, as long as several interferograms are used. Using the joint results, we estimate that each location parameter (X,Y and depth) is accurate to  $\pm 1$  km, and that volume change is accurate to 0.05 units in log space (so that the absolute error scales with the size of the source). There is generally overlap between the misfit functions for each of the elastic media, but the minima can be different on the km-scale, with differences depending on source depth (Figure 2.2).

The mean elevation in the vicinity of the sources of active deformation is as follows: 5 km at Hualca Hualca; 4.9 km at Uturuncu; 4.8 km at Lazufre; and 4.2 km at Cerro Blanco. Local topographic variations can influence the inferred depth of a deformation source, principally because of the variable distance between the source and local relief (*Williams and Wadge, 1998; Cayol and Cornet, 1998; Williams and Wadge, 2000*). A simple and generally effective method of accounting for the topographic effect is to use a source depth for each pixel in an interferogram, perturbed by the local elevation (*Williams and Wadge, 1998*). We use this approximation to estimate source depth at all four actively deforming sources, and find that it changes the inferred source depth by less than 500 m. Thus, the effect of topography upon inferred source depth is less than the uncertainty in depth mentioned above. There is some doubt as to whether it is most appropriate to use the mean elevation, or some other metric (*Williams and Wadge, 1998*), but this uncertainty is also of order 1 km, and already included in our

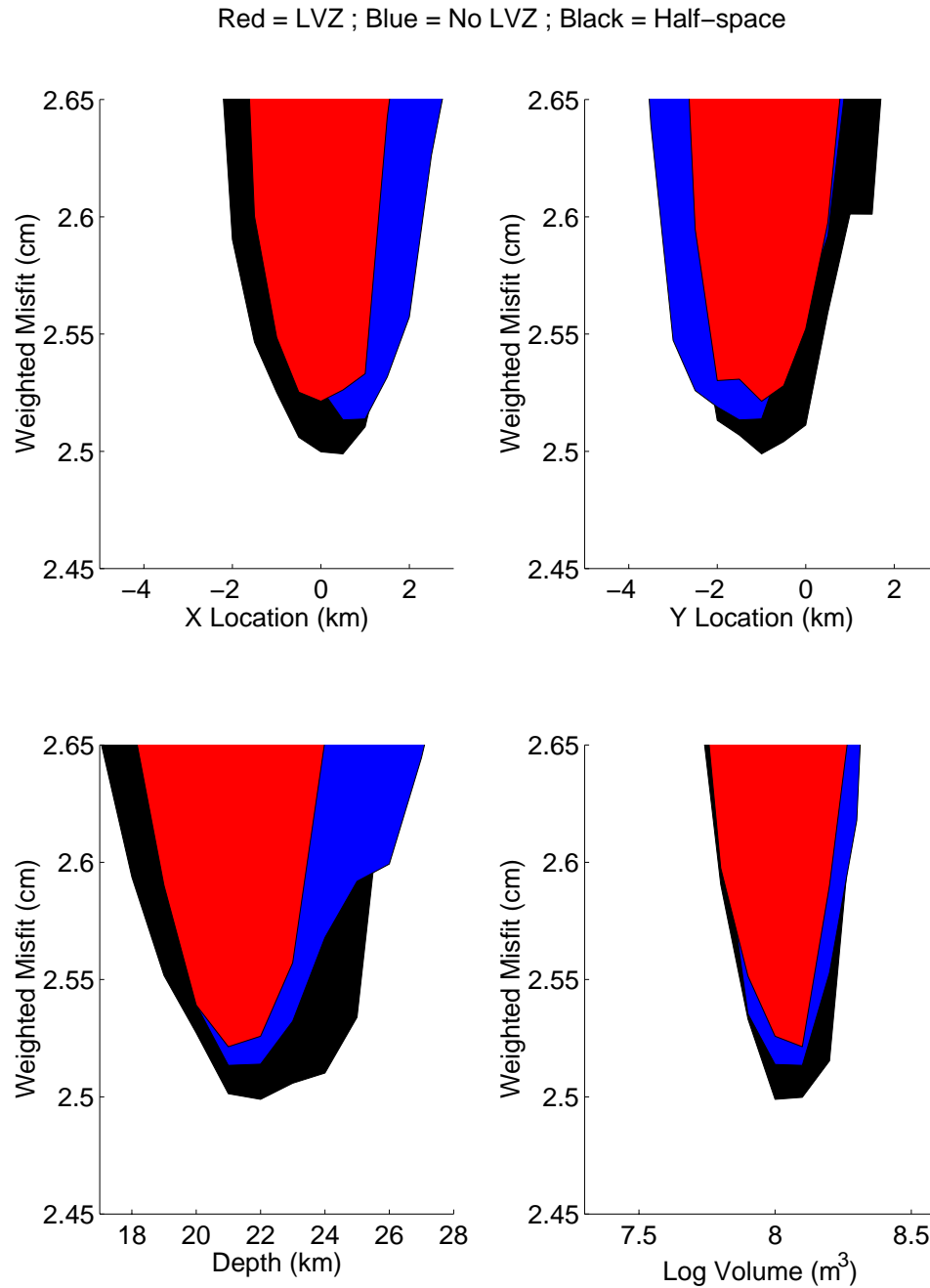


Figure 2.4: Scatter plot output from the NA inversions showing misfit as a function of model parameters for three elastic media – half-space, layered model 1 and layered model 2 (Figure 2.2). The misfit function is based on the L2 norm between data and the model, but is larger than the actual residual because it is calculated using a sub-sampled and weighted dataset derived from our data sub-sampling program (*Simons et al.*, 2002). The depths are below the local reference elevation, and 4900 m should be subtracted to convert the depths relative to sea level. The best fitting depths for the models are: 22.2 km half-space; 21.9 km LVZ; 21.7 km No LVZ.

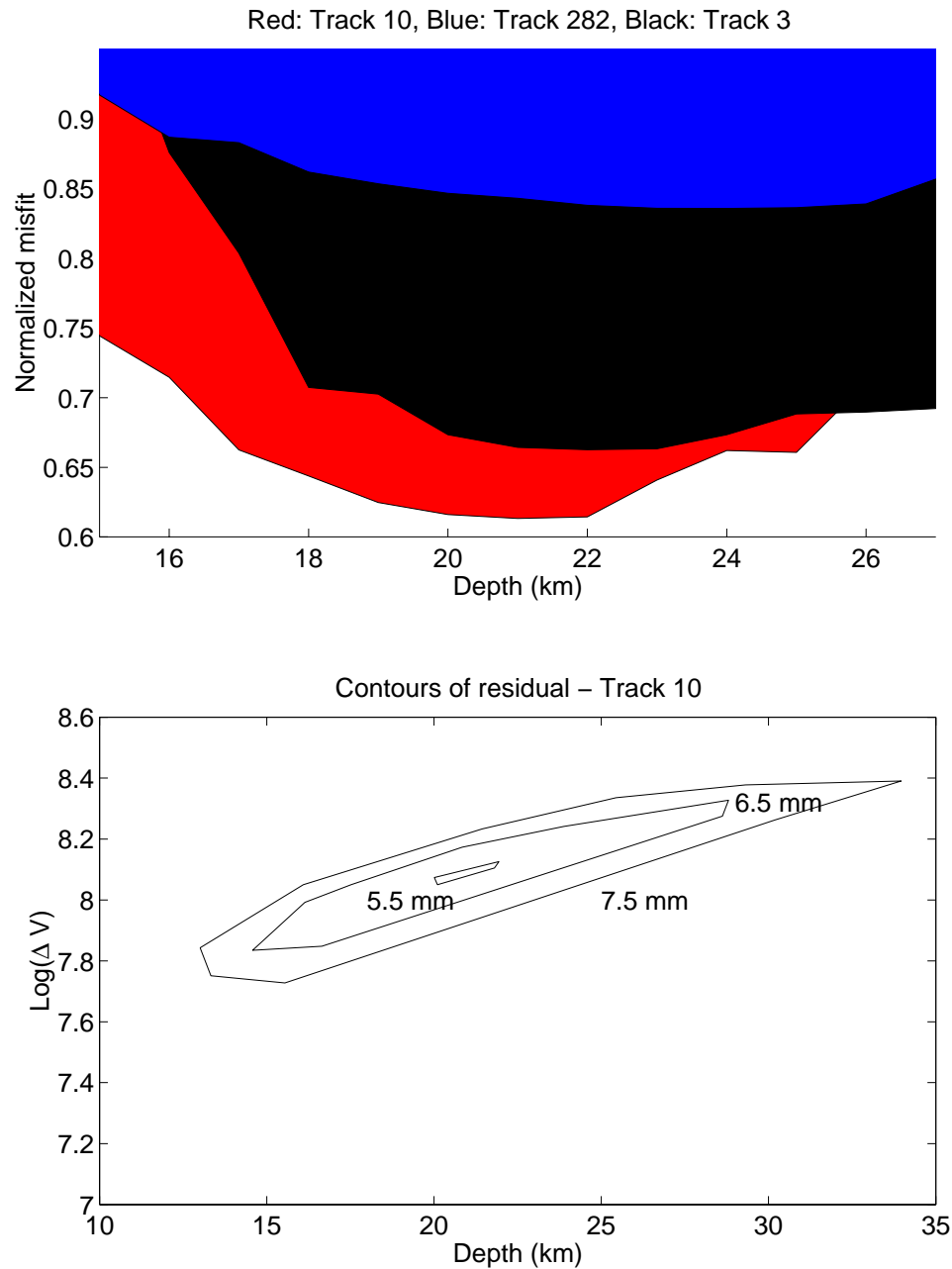


Figure 2.5: (Top) Comparison of inferred source depth from inversion of three different satellite tracks at Uturuncu, done in separate inversions. Black is from ascending track 3, and has a best fit depth of about 22 km (relative to local reference elevation). Red is from descending track 10 with a best fit depth of about 21 km, and blue is from descending track 282 with a best fit depth of 23-24 km. Because the misfit for each orbit is different, the misfits have been normalized by the mean error for ease of comparison. (Bottom) Contours of misfit plotted as a function of depth vs. strength for an inversion using only a single interferogram from track 10 showing the trade-off between source depth and the source strength.

range of depths for each source. Considering the variation due to the elastic media, the effects of topography, and the width of the misfit function, we estimate the depth of a spherical source for Uturuncu to be 16-18 km below sea level (21-23 km below the local surface).

With only a single LOS component of deformation, many assumed source geometries can match the observations (e.g., spherical, prolate ellipsoids, and penny-shaped cracks) (*Fialko et al.*, 2001b). The variations in source geometry effect the inferred source depth. Deformation from a shallow prolate ellipsoid with the semi-major axis nearly vertical can look similar to a deeper ellipsoid with the semi-major axis nearly horizontal (and with a different ratio of the semi-major to semi-minor axis). Because dips within about 20 degrees of horizontal and vertical look similar, we include this range when we refer to horizontal and vertical prolate ellipsoids. Prolate ellipsoids with other dips lie at depths in-between these extremes. For the penny-shaped crack, the shallowest models have a large ratio between crack radius and depth and are called finite cracks. As the ratio of radius to depth decreases and approaches a “point crack,” the depth of the best-fitting source increases. At Uturuncu, we have found that using data from both ascending and descending satellite tracks can restrict the range in dips of the prolate ellipsoids, and constrains a vertical prolate source to have a spherical aspect ratio. All types of models (vertical and horizontal ellipsoids and finite and point cracks) fit the data equally well (Figure 2.6), and the depths of these sources span nearly 10 km (Table 2.2). A wider range of prolate ellipsoids (with dips between nearly vertical and horizontal) are permitted at the other sources because we only have good observations from descending satellite tracks. We have not attempted to determine all source geometries that explain the data, but instead pick end member models to show plausible extremes in source depth (Table 2.2 and Figure 2.7).

Using InSAR deformation data, we can constrain the rate of source volume inflation as a function of time (Figure 2.8). We assume a constant source depth (see Table 2.2 for depths), a spherical source in a half-space, and a constant rate of deformation during the time period covered in the interferogram. The horizontal bar

Volcano		Uturuncu	Hualca Hualca	Lazufre	Cerro Blanco
Location (Lat,Lon)		-22.265,-67.185	-15.73,-71.86	-25.33,-68.52	-26.77,-67.72
Spherical	X	-3.5	1.4	1.2	-0.6
	Y	-2	0.7	6.5	-1.5
	Z	17.3	13	7.3	4.8
Horizontal Ellipsoid	X	-1.5	1.37	1.6	-1.1
	Y	-1.4	1.5	6.1	-1.6
	Z	18.8	12.5	9.8	7
	$\theta$	2.9	1.7	-1.2	0.6
	$\phi$	77.9	91.7	112	244
	a/b	6.4	1.0	9.5	5.7
Vertical Ellipsoid	X	-3.2	-1.3	-2.9	-0.4
	Y	-1.4	1.0	7.6	-0.5
	Z	18.2	7.8	11.2	5.6
	$\theta$	100	77.4	66.0	72.4
	$\phi$	286	90.8	109	233
	a/b	1.0	1.7	4.3	1.2
Point Crack	X	-3.1	9.7	5.6	2.3
	Y	-1.6	-1.0	5.7	-2.3
	Z	25	18.1	12.8	9.7
	radii	0.4	1.1	1.0	1.0
Finite Crack	X	-3.3	3.1	5.4	0.3
	Y	-1.7	4.6	5.5	-1.2
	Z	12	10	5.2	5.8
	radii	21	16.0	13.4	7.4

Table 2.2: List of best fitting source locations for each actively deforming volcano for different source geometries in an elastic half-space. The location of the volcano is the latitude and longitude of the volcanic edifice, X and Y indicate the source location relative to that position, and Z is the depth below sea level. All Z, Y, Z locations and radii are in km. The latitude and longitude for Lazufre is at the center Cordon del Azufre, so the source is NE of that volcano. The volume of inflation or deflation in the source varies between interferograms, see Figure 7. The data from this table (including the location of spherical sources in a layered-space) is shown in Figure 5. The minimum depth of the finite crack is not sharply defined (particularly at Hualca Hualca), and we pick a representative value that explains the data.

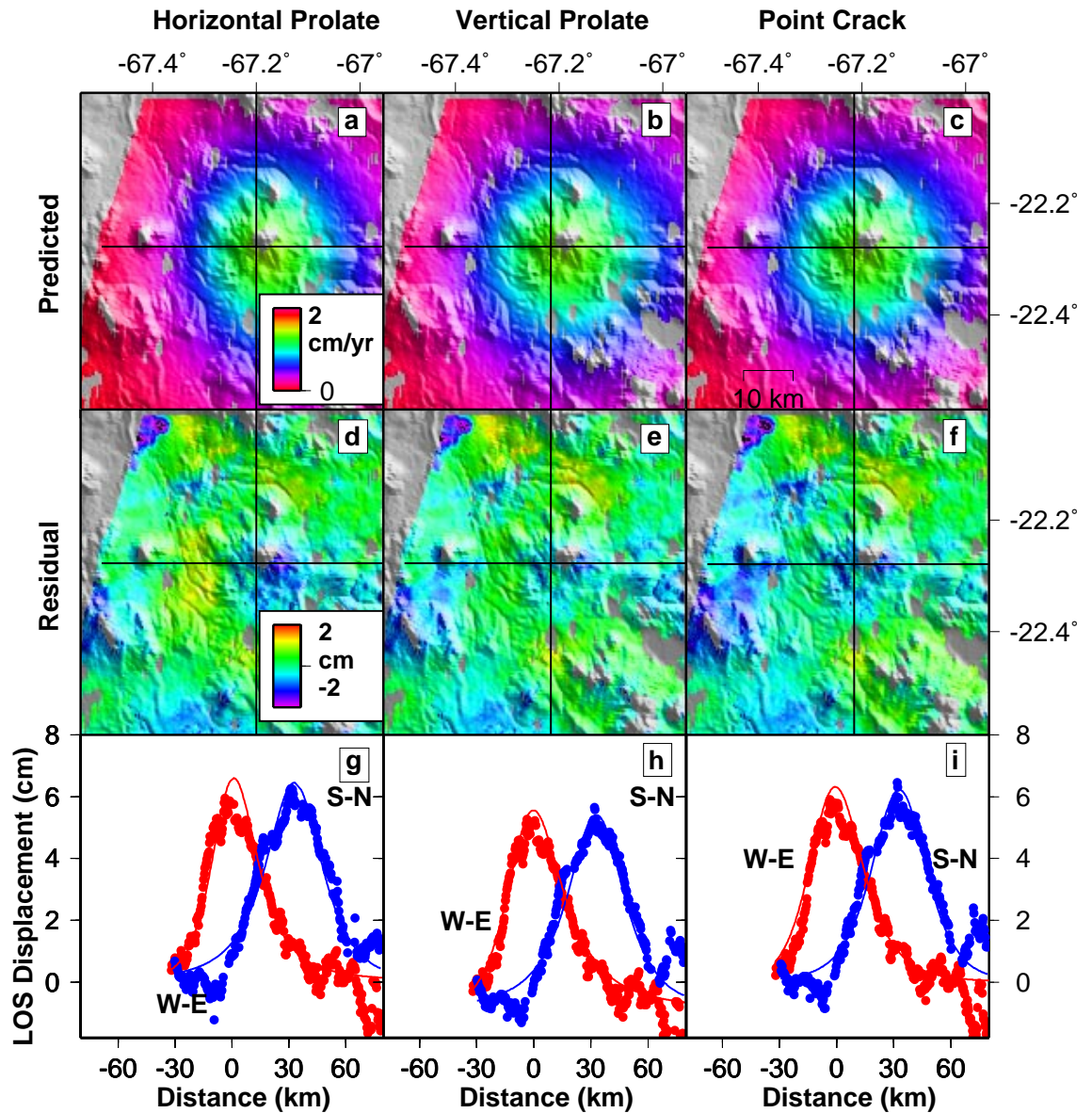


Figure 2.6: a., b., c. Modeled rates of deformation (cm/yr) at Uturuncu from descending track 10 (same data as in Figure 2.3) from different source geometries – a. horizontal prolate; b. vertical prolate; c. point crack. Results for a spherical point source in a half-space are shown in Figure 2.3. Black lines are location of profiles shown in the bottom row of the figure. d., e., f. Residual between data and model, shown as displacement. g., h., i. South-north and west-east profiles through the model and data, where the south-north profile has been offset for the sake of clarity.

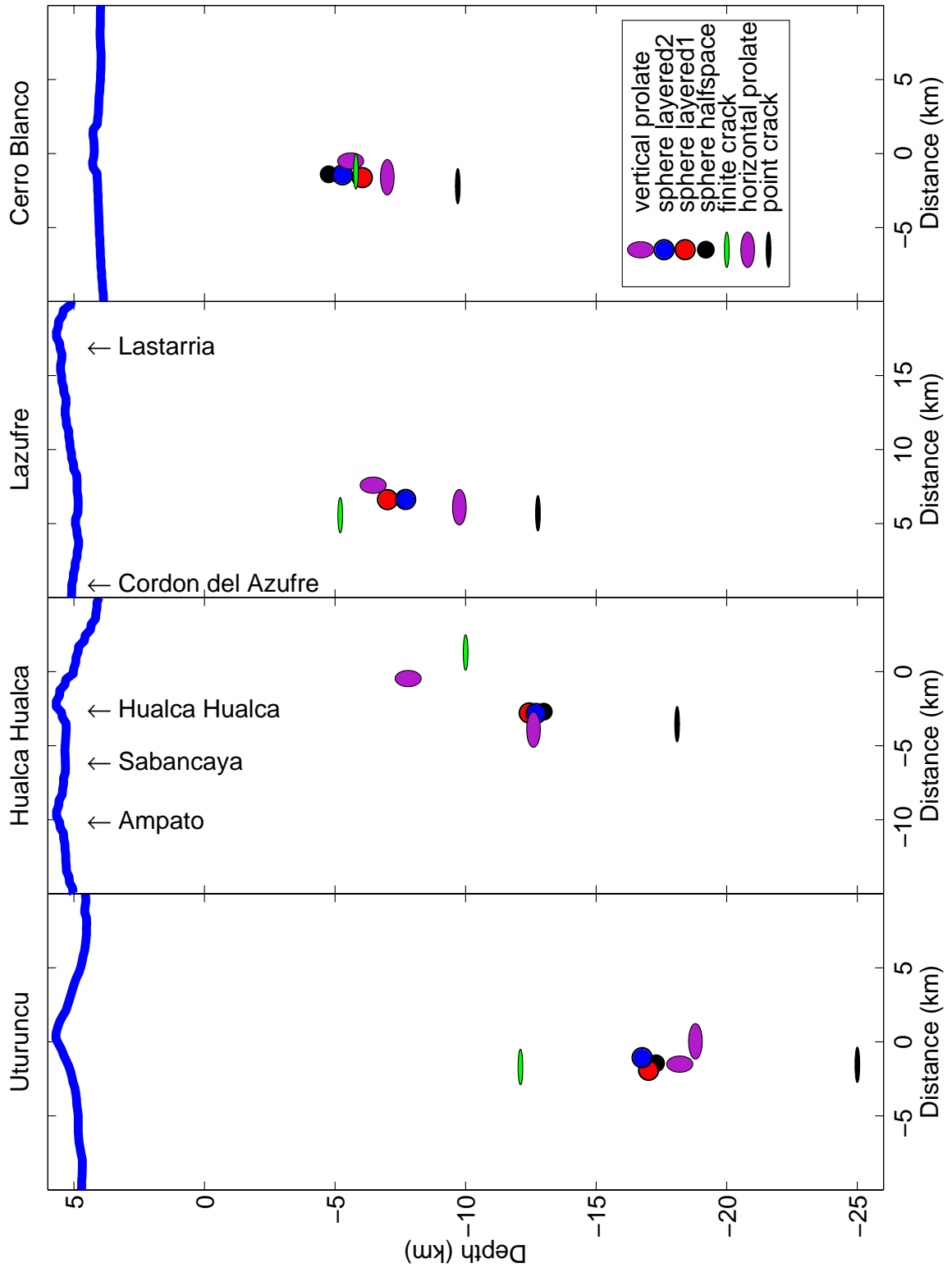


Figure 2.7: North-south profiles at the four deformation centers showing the topography and the inferred location and depths for the spherical, ellipsoidal and crack sources of deformation. The ellipsoidal and crack sources spherical sources were calculated in a half-space while the spherical sources were calculated using both layered- and half-space crustal models.

shows the timespan of the interferogram and the vertical bar reflects an estimate of the error on the inferred rate of volume change. The error bar is 0.05 units in log space (so that the absolute error scales with the size of the source), except for InSAR scenes with extensive atmospheric contamination at Hualca Hualca where the error was estimated to be 0.10 log units (see below). The vertical error bar has been estimated by examining the spread in the scatter plot of misfit as a function of source strength, comparing the strength results from inversions of different combinations of datasets, and comparing interferograms that span nearly the same time interval, including a set of interferograms at Cerro Blanco that differ by only 1 day (made using a tandem pair). There is a suggestion that the inferred rate of volume change in the magma chamber below Uturuncu slightly increases in inflation rate after early 1998 (Figure 2.8, *Pritchard and Simons, 2002*). An increase at about the same time is more apparent at Lazufre and is discussed more below. At a given source depth, the inferred volume change depends only slightly on source geometry, and the majority of our best best-fitting non-spherical sources lie within the plotted error bars. Of course, because of the trade-off between source depth and strength, if the model is at one of the extremal values (e.g., finite or point crack) all of the volumes in Figure 2.8 could be shifted up or down by a factor of 2 or less (depending on the deformation center).

There is a further source of ambiguity regarding the depth and volume of the magma chamber, because if deformation is caused by mass migration, the sources are not monopoles, but dipoles. In other words, while we have used surface deformation to constrain the location of the inflation source, if the inflation is caused by magma injection, there must also be a source of deflation affecting the surface deformation. Of course, it is possible that the inflation we infer is not the result of magma movement as we discuss in the conclusion. If the sources of inflation and deflation (the dipole) are close together and nearly the same shape, the surface deformation pattern can be strongly affected, such that the inferred source depth and volume change will be inaccurate. For the interferograms of Hualca Hualca and Uturuncu, we infer about  $10^8 \text{ m}^3$  of magma to moving at depth, and if all of this material is removed from a

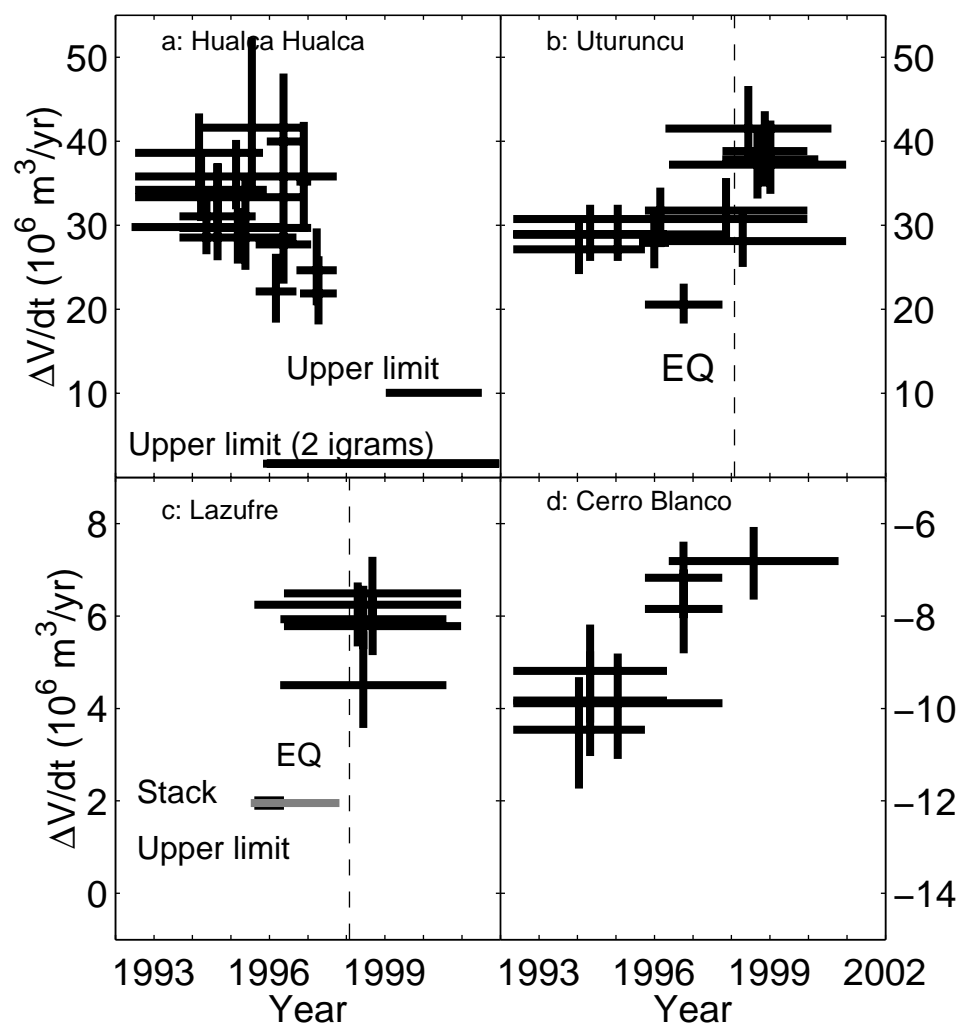


Figure 2.8: Inferred rate of volume change as a function of time, assuming a constant source depth at each location, a spherical source in a half-space, and a constant rate of deformation during the time period covered in the interferogram. The horizontal bar shows the time period covered by the interferogram and the vertical bar reflects an estimate of the error on the inferred rate of volume change. See text for discussion of errors and inversion details. a. Hualca Hualca shows nearly constant deformation between 1992-1997 (with a possible decrease in rate starting in 1996) and no obvious deformation between 1997-2001. b. There is a suggestion of an increase in inflation at Uturuncu following a 1998  $M_w$  7.1 earthquake (shown as dotted line), but a constant rate is not rigorously excluded. c. At Lazufre, no deformation is observed in 2 stacked interferograms before 1998, while interferograms that include times after 1998 show deformation. The  $M_w$  7.1 Chilean subduction zone earthquake (dotted line) might be related to the initiation of inflation (see text). d. Cerro Blanco appears to have a decrease in deflation as a function of time – note change in sign of deformation relative to other sources, and different scale used on each ordinate.

spherical chamber, the effects of this removal should be observable if the chamber is less than about 40 km deep (Figure 1.7). Our preliminary tests of the dipole effect for Hualca Hualca, Lazufre, and Uturuncu indicate that the most important implication is that we might have underestimated the volume of magma that moved. The dipole effect would be reduced if the source of deflation was broad and diffuse – *i.e.*, the magma was collected from a large reservoir or series of channels. A better understanding of the magma plumbing system from seismic tomography is needed to assess the importance of the dipole effect.

### 2.3.2 Hualca Hualca

We show the data, model, residual and profiles for Hualca Hualca from three interferograms from a single satellite track in Figure 2.9. Within error, Hualca Hualca has a constant rate of inflation prior to 1997, although a decreased rate starting in 1996 is possible (Figure 2.8). No deformation is seen in three interferograms spanning times after 1997. Of all the deformation centers we observed, atmospheric contamination was most evident in a few interferograms from Hualca Hualca. As an example, Figure 2.10 shows the correlation of residual phase with topography at Chachani volcano, about 30 km from Hualca Hualca. Several factors suggest that this signal is due to atmospheric effects: (1) the residual appears in some interferograms, but not others that cover nearly the same time interval (Figure 2.10); (2) The signal changes sign in temporally overlapping interferograms; (3) The magnitude of the signal seems to be independent of the time interval.

To model the source of deformation, we first used the three independent interferograms in Figure 2.9 that showed no significant correlation between variations in phase and topography to constrain the source location. Using the calculated location, we inverted the interferograms with atmospheric artifacts for source strength and a ramp with topographic dependence (*i.e.*, solved the equation  $\phi(x, y, z) = ax + by + cz + d$ , where  $x$ ,  $y$  are horizontal coordinates and  $z$  is the elevation), a technique that has been used in other parts of the world (e.g., *Feigl et al.*, 2002; *Hoffmann*, 2003). The

parameter  $c$  is of order 1-1.5 cm/km, and does not explain all of the tropospheric signal in Figure 2.10, since the signal is not purely correlated to topography. Because there is a potential trade-off between  $c$  and the inferred volume change, there are larger errors in our estimates of volume change for interferograms with obvious atmospheric contamination (Figure 2.8).

A region of localized subsidence can be seen in the raw data, residual and south-north profiles, to the N-NE of Hualca Hualca (Figure 2.9a.,b.,g.,h.,j., and k.). Figure 2.11 shows a zoom in on the residual at Hualca Hualca draped over topography in the region of localized subsidence. The region labeled “residual anomaly” is about 2 by 2 km centered on 15.69°S, 71.83°W, and has an amplitude of between 1-3 cm. There might actually be a surface break, but the truncated phase could also be due to the extreme topography in the area. A smaller source (amplitude  $\sim$  1 cm) is observed in some interferograms located roughly due west, also about 2 by 2 km, centered on 15.67°S, 71.89°W. Both sources of deformation are seen in several interferograms, but because of our limited data coverage, we cannot rule out that both sources are due to earthquakes during the common time period (8/24/1995-8/31/1993). Figure 2.11 shows the cataloged earthquakes closest to the deformation during the time period, with the earthquake on 12/26/1994 being the most plausible candidate. Our inversion for the source gives  $M_w$  4.7, close to the catalog moments ( $M_b \sim$  4-5, see Figure 2.11), and a mechanism similar to the Harvard CMT solution. However, our location is 10-45 km from the catalog locations and our depth is only 1.4 km, compared to 10-44 km in the catalogs. See Chapter 1 for a discussion of the inversion method and ambiguity of model parameters. Alternatively, the residual could be related to fumarolic activity (reported for Hualca Hualca, *Gonzalez-Ferran*, 1995), whether through localized ground subsidence or through the higher local concentrations of water vapor (as suggested for the hydrothermal plant at Cerro Prieto, Mexico, *Hanssen*, 2001). A less likely possibility is a shallow dike intrusion.

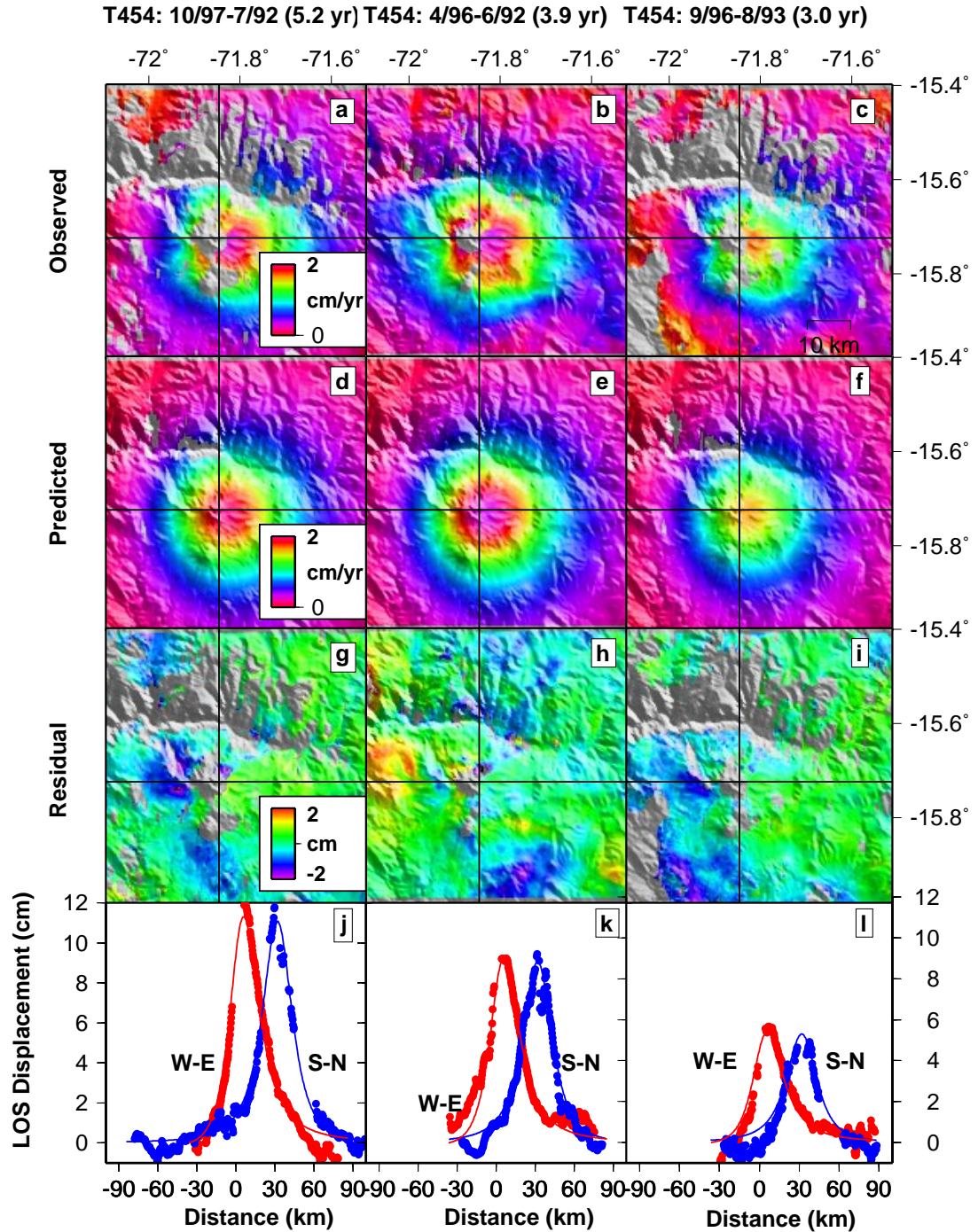


Figure 2.9: Observed (a., b., c.) and modeled rates (d., e., f.) of deformation (cm/yr) at Hualca Hualca in three independent interferograms, all taken from the same track of descending InSAR data. Black lines show location of profiles shown in the bottom row of the figure. The interferograms on the left and in the center show small region of localized subsidence on the north flank of Hualca Hualca, while this region is decorrelated in the interferograms on the right. See Figure 2.11 for more detail. g., h., i. Residual between data and model, shown as displacement. j., k., l. South-north and west-east profiles through the model and data, where the west-east profile has been offset for the sake of clarity.

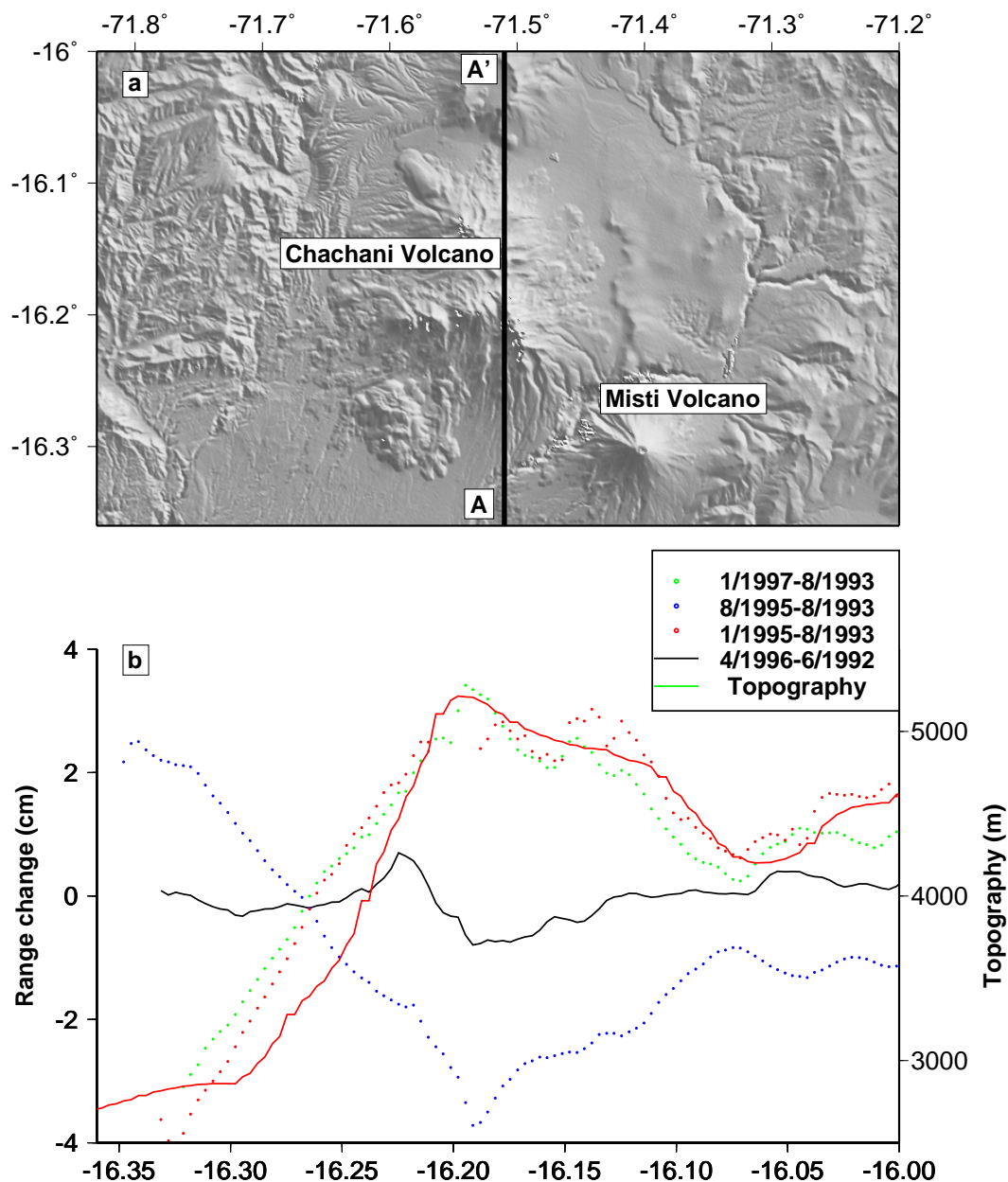


Figure 2.10: Profiles through several interferograms in southern Peru (track 454, frame 3925) showing residual phase correlated with topography, presumably related to atmospheric effects. a. Regional topography near location of profiles (black lines) over Chachani volcano about 30 km SE of Hualca Hualca. b. Profiles from 4 interferograms and topography. Dotted lines are from interferograms that show a correlation between range change and topography and the solid line is from an example interferogram with little correlation between range change and topography.

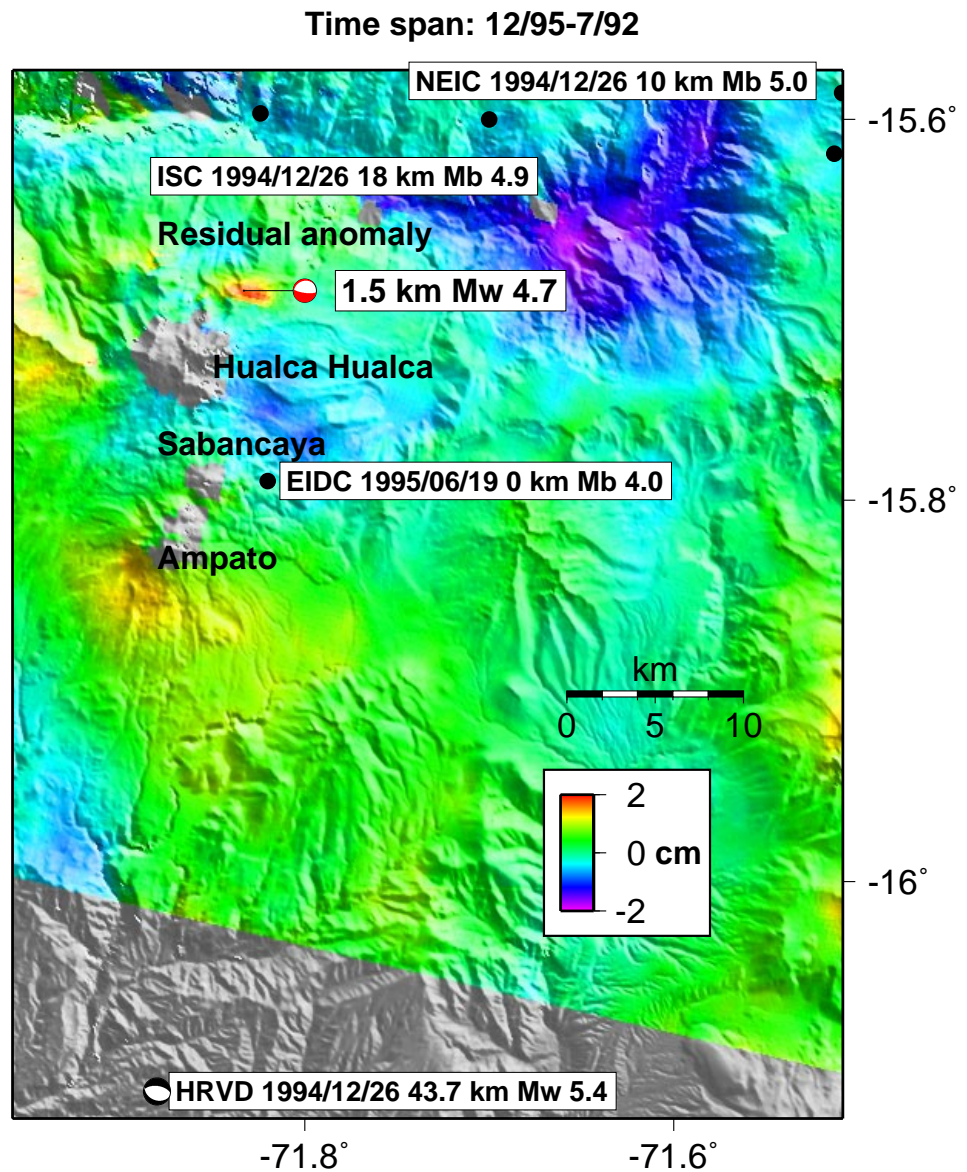


Figure 2.11: Residual (data-model) for an interferogram spanning 12/1995-7/1992 showing an anomaly NE of Hualca Hualca, which is modeled as an earthquake (red mechanism). The closest earthquakes in the ISC and other catalogs during the time period during which the deformation occurred are shown as black dots. The closest event in the Harvard CMT catalog is shown as a black mechanism. The ISC locations for the event on 6/19/1995 is off of this map and at 165 km depth, so we think the most plausible earthquake source for the deformation was the event on 12/26/1994. Of course, the deformation might not be due to an earthquake (see text).

### 2.3.3 Lazufre

Figure 2.12 shows data, model, residual and profiles for two interferograms at Lazufre. Compared to predictions from a spherical model, the observed deformation looks slightly aspherical, with a NE-SW axis. The best-fitting prolate ellipsoid improves the fit, but the decrease in residual (about 5%) is small considering the number of additional parameters used (e.g., five for the spherical source versus nine for the ellipsoidal source when only a single interferogram is used).

Figure 2.8 shows the inferred volume change in the magma source region over the time period when data was available (7/1995-12/2000). Unfortunately, only one track of radar data is available (with seven interferograms) for Lazufre, and this track has only limited temporal coverage. However, even with this limitation, the data suggest time-dependence of the deformation, with no deformation apparent in two stacked interferograms before the beginning of 1998, and a clear signal in three interferograms after that time. The temporal coverage is insufficient to resolve whether the start of deformation was abrupt or gradual. We note that there also seems to be a slight increase in the rate of inflation at Uturuncu, at about the same time. While the inflation rate increase could be a coincidence, because the increase occurs at the two centers at about the same time, there might be some external triggering process. We note that a  $M_w$  7.1 subduction zone earthquake occurred near the time of the increase (January 30, 1998), and that unrest at volcanic centers has been triggered by earthquakes before (e.g., *Johnston et al.*, 1995). Of the deforming volcanoes we observe, Uturuncu and Lazufre are the closest to this earthquake (about 400 and 300 km, respectively). None of the volcanoes were obviously effected by the  $M_w$  8.1 Antofagasta earthquake (July 30, 1995) in about the same location as the 1998 event.

### 2.3.4 Cerro Blanco (Robledo)

The data, model, residual and profiles for three interferograms from two different satellite tracks at Cerro Blanco spanning 5/1992-10/2000 are shown in Figure 2.13. The rate of subsidence seems to decrease with time from a maximum of more than

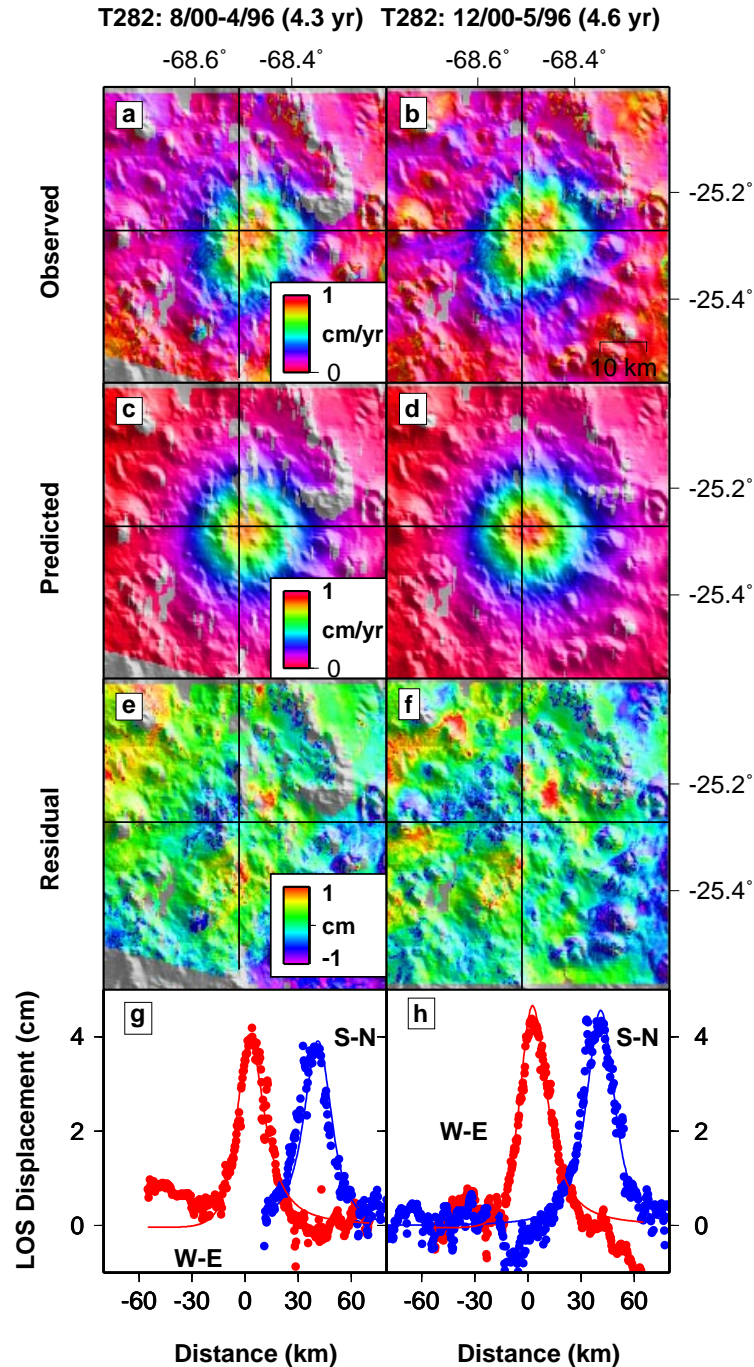


Figure 2.12: Observed (a., b., c.) and modeled rates (d., e., f.) of deformation (cm/yr) at Lazufre (between Lastarria and Cordon del Azufre) in two independent interferograms, taken from the same track of descending InSAR data. Black lines are location of profiles shown in the bottom row of the figure. g., h., i. Residual between data and model, shown as displacement. The are small, consistent residuals NE and SW of the deformation center, and these features remain even with the best-fitting axisymmetric prolate and oblate sources. We suspect that the residual is either atmospheric contamination related to topographic changes. j., k., l. South-north and west-east profiles through the model and data, where the west-east profile has been offset for the sake of clarity.

2.5 cm/yr in the radar LOS (interferograms spanning 1996/7-1992) to less than 1.8 cm/yr (2000-1996), which translates into a deceleration in the rate of source volume change (Figure 2.8).

#### 2.3.4.1 Physical cause of subsidence

Several mechanisms have been proposed for subsidence at calderas – cooling and solidification of magma, regional extension, and removal of hydrothermal or magmatic fluids with concomitant compaction (e.g., *Newhall and Dzurisin*, 1988). Without knowing the history of uplift and subsidence at Cerro Blanco or the characteristics (or existence) of its hydrothermal or magmatic system, it is difficult to constrain the source of the subsidence. Here we outline some simple physical arguments suggesting that conductive cooling and crystallization of a magma chamber alone can not explain the rate of subsidence at Cerro Blanco. We posit the existence of a hydrothermal system to increase the cooling rate and/or to cause subsidence through poroelastic effects.

Tectonic extension and magma withdrawal are unlikely explanations for the subsidence at Cerro Blanco. Several authors have proposed that tectonic activity controls caldera collapse and shallow magma movement in the central Andes (e.g., *Riller et al.*, 2001), and much tectonic activity is located at the southern end of the arc near Cerro Blanco (*Gonzalez-Ferran et al.*, 1985). However, the existence and magnitude of regional extension that might be localized by weakening effects of a magma body (as proposed for Yellowstone and Medicine Lake, *Dvorak and Dzurisin*, 1997) is unknown. Magma withdrawal was probably not horizontal because we do not see any nearby areas of inflation (such as seen at Aira and Sakurajima, Japan, *Tada and Hashimoto*, 1989), although if such movement was diffuse it would be hard to detect. Magma cooling and solidification both involve contraction which can lead to surface subsidence. Conductive cooling is an inefficient process, especially because as cooling progresses, the immediate surrounding material warms up and the rate of heat loss diminishes. If Cerro Blanco has a hydrothermal system (none has been documented), the flow of liquid water and steam can significantly increase heat loss. Modeling the

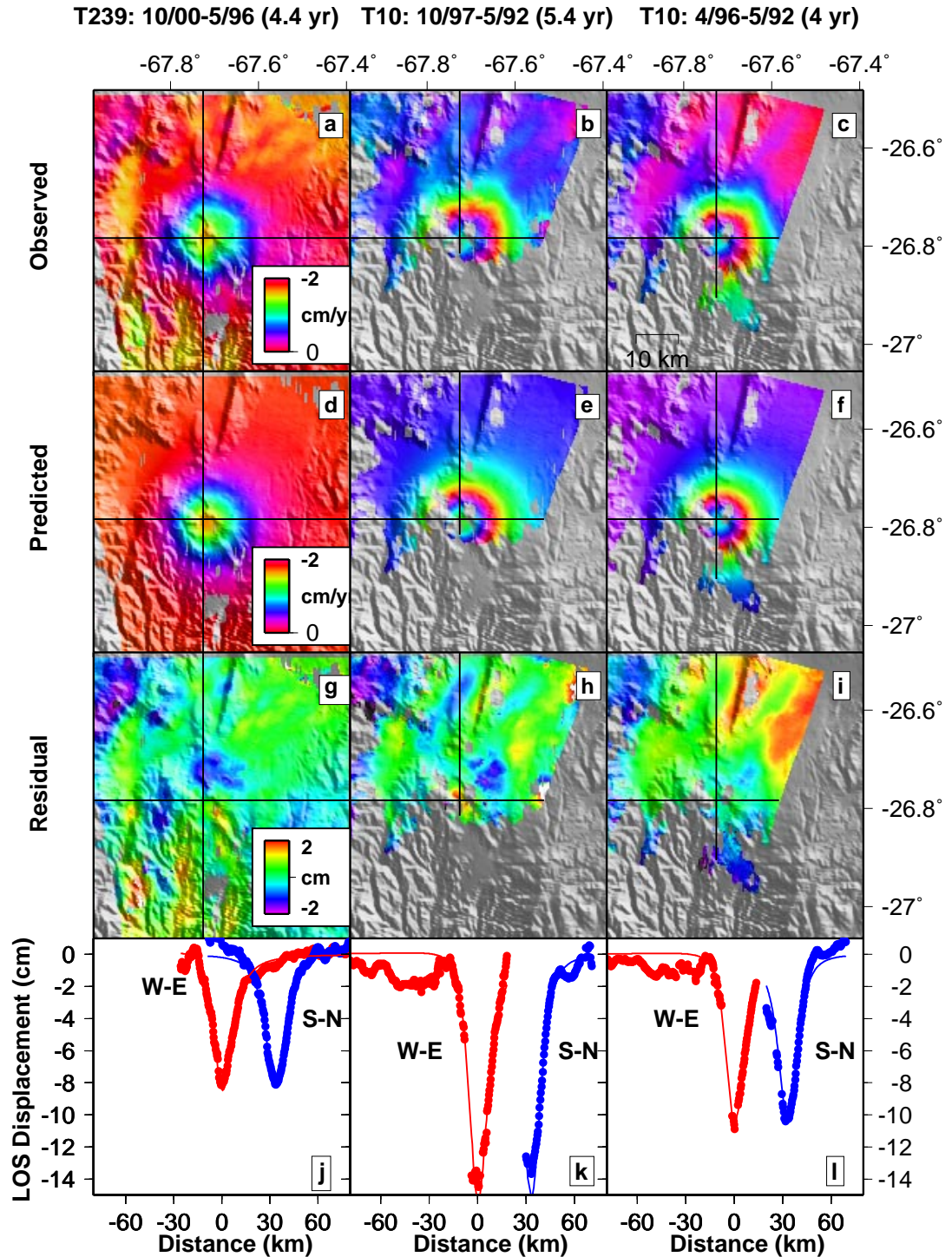


Figure 2.13: Observed (a., b., c.) and modeled rates (d., e., f.) of deformation (cm/yr) at Cerro Blanco in three interferograms, taken from two tracks of descending InSAR data. Black lines are locations of profiles shown in the bottom row. g., h., i. Residual between data and model, shown as displacement. j., k., l. South-north and west-east profiles through the model and data, where the west-east profile has been offset for the sake of clarity.

deformation of coupled magmatic/hydrothermal systems is complicated because the calculations involve many unconstrained parameters (e.g., *Bonafede, 1991; Jousset et al., 2000*), although our calculations below motivate future work on the problem for Cerro Blanco.

To explore a conductive cooling model for the observed subsidence, we first give some order of magnitude arguments and then some results of one-dimensional numerical modeling. We first assume the magma started at the melting point ( $\sim 1100$  K) and cooled to ambient conditions at a depth of 10 km (we assume a geothermal gradient of 30 K/km, a conservative choice because average heat flow in the western cordillera is 80 mW/m<sup>2</sup> and can exceed 100 mW/m<sup>2</sup>, *Giесе, 1994*). A relative volume change of  $\alpha\Delta T \sim 1\%$  is possible, where  $\alpha$  is the coefficient of thermal expansion ( $2 \times 10^{-5}$  K<sup>-1</sup>), and  $\Delta T$  is the temperature difference between the solidus and ambient conditions. Given this volume change, a volume of  $1 \times 10^9$  m<sup>3</sup>/yr is required to explain the subsidence at Cerro Blanco. For these order of magnitude arguments, we assume the conditions most favorable to cooling – that the ambient conditions begin and remain cold, so that we can use the diffusion relation ( $\sim \sqrt{(\kappa t)}$ , where  $t$  is time and  $\kappa$  is thermal diffusivity  $1 \times 10^{-6}$  m<sup>2</sup>/s) to estimate the amount that can cool each year (a region of order 1-10 m thick). Using a thickness of 1-10 m would require a magma chamber of radius greater than 5-15 km to explain the observed subsidence. Solidification of magma involves a larger volume change than cooling for a given amount of heat flux (Q) as can be seen by comparing the fractional volume changes for the two processes:

$$\frac{(\frac{Q}{L} * \rho) * \Delta\rho}{(\frac{Q}{C_p * \Delta T * \rho}) * \rho * \alpha * \Delta T} = \frac{C_p * \Delta\rho}{L * \alpha * \rho} \sim 10, \quad (2.1)$$

using appropriate numbers for L (latent heat =  $4 \times 10^5$  J/kg),  $C_p$  (specific heat =  $4 \times 10^5$  J/kg/K), the density change upon solidification ( $\Delta\rho \sim 250$  kg/m<sup>3</sup> - about 10% volume change, *Sigmundsson et al., 1997; Fialko et al., 2001c*), density ( $\rho \sim 3000$  kg/m<sup>3</sup>) and the other parameters as given above. Because of the greater efficiency, a volume of magma equivalent to about  $1 \times 10^8$  m<sup>3</sup>/yr must crystallize,

requiring a chamber radius of 1-3 km assuming, as above, the most favorable cooling conditions of a region 1-10 m crystallizing.

To get a more realistic estimate of the chamber radius required, we have done numerical simulations of one-dimensional spherical conductive cooling (accounting for phase changes) using a finite difference method (see *Toksöz and Solomon, 1973*, for the equations used). There are at least three different scenarios for conductive heat loss with different consequences for the rate of cooling and volume change. The most efficient heat loss configuration is if the magma chamber is fluid, convecting and isothermal, and conducts heat into the surrounding medium (*Marsh, 1989*). Heat loss from the isothermal magma chamber can be twice as great as from a non-convecting magma chamber (*Marsh and Maxey, 1985*). As the magma chamber starts to crystallize, its viscosity increases and convection becomes less vigorous, but for the timescales and magma volumes we are interested in, the amount of crystallization is small. The other two scenarios are a non-convective, liquid magma chamber and a non-convective solid magma chamber, and have different amounts of volume change per unit cooling. We have tested all three scenarios for conductive cooling, and found that a chamber radius of more than 17 km would be required to achieve the observationally required volume. The value is larger than the order of magnitude estimates partly because there is a trade-off between warming (and thermally expanding) the surrounding country rock and cooling (and thermally contracting) the magma chamber. In fact, under certain (cold) ambient conditions, uplift of the ground surface is possible. Such a large radius requires at least an equal depth for the source, and is not consistent with our observations of a source depth between 9-14 km. Of course, the surface deformation pattern is affected by the finite size of the magma chamber, but when we do inversions accounting for this effect (using the corrections of, *McTigue, 1987*), we still find a source depth of 11 km. Furthermore, a chamber 17 km in radius is probably implausibly big (for example, it would have 20 times the volume of the inferred magma chamber in Long Valley caldera, California, *McTigue, 1987*).

In addition to the arguments about the absolute rate of cooling given above, the change in the rate of cooling can help constrain the physical processes involved.

During the period of observation, the rate of cooling decreased by a factor of two over about five years. It is difficult to achieve this change in the rate of cooling solely by conduction unless there was an intrusion at Robledo a few years before the observations began in 1992, which is not implausible.

Cooling and/or crystallization of a magma chamber by conductive processes alone is therefore unlikely to be the cause of the observed deformation, and a hydrothermal system must exist. This is not surprising, since at other calderas, the removal of fluids is the favored cause of subsidence (e.g., Yellowstone and Campi Flegrei, *Dvorak and Mastrolorenzo, 1991; Dvorak and Dzurisin, 1997; Dzurisin et al., 1999*), although all these authors acknowledge that there the exact cause of the deformation is uncertain. Fluids (gas and brine) exsolved from the cooling magma body could be removed allowing compaction and subsidence of the previously fluid-filled pores (*Dvorak and Mastrolorenzo, 1991*). Alternatively, or concurrently, a hydrothermal system could become self-sealed and pressurized by the fluids causing inflation, or subsidence when the seal is broken (*Dzurisin et al., 1999*). The inferred depth of activity at Cerro Blanco (9-14 km) is similar to that at Yellowstone ( $8.5 \pm 4$  km, *Wicks et al., 1998*) but deeper than at Campi Flegrei (3 km, e.g., *Dvorak and Mastrolorenzo, 1991*). Ultimately, discriminating between hydrothermal and magmatic activity as the principle cause of subsidence requires repeated microgravity observations to constrain the density (*Berrino et al., 1992; Battaglia et al., 1999*), but studies of the history of uplift and/or eruptions at Cerro Blanco and confirmation of the existence of a hydrothermal system are also needed.

## 2.4 Mass balance in a volcanic arc

Many workers think that volcanic arcs are areas of continental crustal growth, and have used estimates of the rate of volcanic output to constrain additions to the crust (e.g., *Francis and Rundle, 1976; Thorpe et al., 1981; Rymer and Schubert, 1984; Francis and Hawesworth, 1994*). Constraining the rate of crustal growth is important for understanding the evolution of mountain belts and continents. For example, the

rate of volcanic output (and implied crustal growth) is incapable of explaining the crustal thickening of the central Andes during the past 10 Ma, so that another process (tectonic shortening) must be more important (*Allmendinger et al.*, 1998). Converting volcanic output to crustal growth is difficult because several important parameters are poorly constrained. For example, while determining the rate of volcanic output is logically straight forward (by accounting for the volumes and ages of subaerial eruptive products), in practice, even the volumes of recent eruptions are only known to an order of magnitude or so. A further complication is that several types of arc volcanism must be considered (from individual andesitic volcanoes in the western cordillera, to diffuse silicic calderas further east, *Francis and Hawesworth*, 1994) and that the occurrence of these centers varies along arc strike (*Baker and Francis*, 1978). To convert volcanic output to crustal addition, the ratio of intrusive to extrusive eruptive products ( $R_{I/E}$ ) is required. In addition, the fraction of the magmas that are due to real additions of material from the mantle as opposed to remelting of pre-existing crustal material must be known. Both of these numbers are poorly constrained.

Our survey of deformation and presumed magma movements within the central Andean arc over the course of a decade can provide an observational constraint on the current  $R_{I/E}$ . There is no technique, geodetic or otherwise, that can be directly used to address the ultimate source of the magmas. Silicic melts in the central Andes can be the result of mafic intrusions from the mantle that subsequently melt crustal material, or from increased mantle heat flow that might plausibly accompany lithospheric delamination (*Babeyko et al.*, 2002). The former implies that all melts are ultimately related to crustal growth while the later does not (*Francis and Hawesworth*, 1994). It is not presently possible to access the relative importance of each process. Geochemical analyses are subject to multiple interpretations and probably can not supply quantitative constraints (*Davidson et al.*, 1991).

Our observations of deformation can be used to estimate the volume of magma intruded into the central Andean volcanic arc, given some assumptions. Our estimates of intruded volumes are lower limits, because magma intrusions might not manifest themselves as detectable surface deformation, particularly if the injection is deep

and/or the volume change is small. Figure 1.7 shows the smallest volume that can be detected at a given depth, assuming a spherical source and that we can detect a signal with a 1 cm maximum amplitude. Our volume estimates are also a lower limit because magma movements might not cause surface deformation if the conduit behaves rigidly or magma fills void space. We assume that surface inflation is entirely due to magma injection, and not from hydrothermal processes or an increase in gas pressure within the magma chamber. While neglecting these other processes might overestimate the volume of magma intruded, the fact that we also neglect magma compressibility, which can accommodate some of the intruded magma without causing surface deformation (*Johnson et al.*, 2000) will serve to underestimate the intruded volume. It is difficult to know how these different processes will trade off, so we make the simplifying assumption that all intruding magma (and only magma) causes surface deformation. For this reason, we neglect the subsidence of Cerro Blanco caldera, which is likely due to cooling/crystallization from a previous injection coupled with hydrothermal activity. In order to relate surface deformation to a volume of magma intruded requires a model for the shape of the source, because the ratio of surface volume change to source volume change depends on source geometry (*Delaney and McTigue*, 1994). Finally, because of limits on data availability, we do not have data for every edifice during the entire time period when radar observations were made. Table 1.1 summarizes the temporal coverage available at volcanic edifices of different ages. For example, we surveyed 91% of the 390 volcanic edifices thought to have been active in the last 1-2 Ma (the ages are poorly constrained) for an equivalent of about 2300 volcano-years. We assume that our survey is complete enough to allow for a lower limit upon the annual rate of crustal deformation and inferred magmatic intrusion.

Given all of these assumptions, the lower bound of the volume of magma intruded in the central Andean arc is  $4\text{-}6 \times 10^{-2} \text{ km}^3/\text{yr}$  for spherically shaped intrusions or  $2.6\text{-}5 \times 10^{-5} \text{ km}^3/\text{yr}$  per km of arc length. Over a similar timespan (1990-2000), between about  $0.9\text{-}4.6 \times 10^{-5} \text{ km}^3/\text{yr}/\text{km}$  of material was erupted in the central Andes. This range in values corresponds to eruptions in the Smithsonian database (*Smithsonian Institution*, 2003; *Simkin and Siebert*, 1994), with additional volume

constraints for large eruptions (*Thouret et al.*, 1995; *Deruelle et al.*, 1996; *Smithsonian Institution*, 1994c). Because all of the eruptions were explosive, the actual dense rock equivalent volume of this material is less, perhaps by a factor of 2-3, meaning that  $R_{I/E}$  is between 1-10. It should be remembered that this calculation only considers the measured input and output of the arc over about a 10 year period. The mass that was intruded during an earlier time and extruded in eruptions at Lascar (and elsewhere) is not considered, nor is volume of material intruded during this time interval that might be extruded in the future. Previous calculations of  $R_{I/E}$  from the central Andes were made by comparing the volume of volcanic rocks to batholithic rocks (*Francis and Rundle*, 1976) or estimating the amount of fractional crystallization (*Francis and Hawesworth*, 1994) are also between 1-10, with the low values corresponding to andesitic melts and the higher values to more silicic melts (*Francis and Hawesworth*, 1994). Values of  $R_{I/E}$  between 1-10 have also been reported in many other arcs (e.g., *Crisp*, 1984).

Volcanic eruptions in the central Andes are strongly episodic, and so we need to consider whether a decade of observations is sufficient to characterize the long-term rate of volcanic input and output. For example, large eruptions are volumetrically the most important (*Pyle*, 1995). The largest historic eruption in the central Andes was in 1600 (*Thouret et al.*, 2002; *Adams et al.*, 2001). Figure 2.14 shows that although time averaging effects might exist, the rate of volcanic output averaged over different timescales (10-10<sup>7</sup> years) is consistent within an order of magnitude, which is within the uncertainty of the individual estimates. It is more difficult to estimate rates of magmatic intrusion over different timescales, particularly because the subsurface shape and age of batholiths are poorly known and it is difficult to determine erosion rates. Our values of  $2.6-5 \times 10^{-5}$  km<sup>3</sup>/yr/km are within an order of magnitude of geologic averages for the coastal batholith of Peru used as an analog for the current central Andean arc ( $0.3-2.6 \times 10^{-5}$  km<sup>3</sup>/yr/km, *Francis and Rundle*, 1976). Therefore, given all of the uncertainties involved, our 10 year study of magma intrusions and extrusions is consistent with the geologic rates.

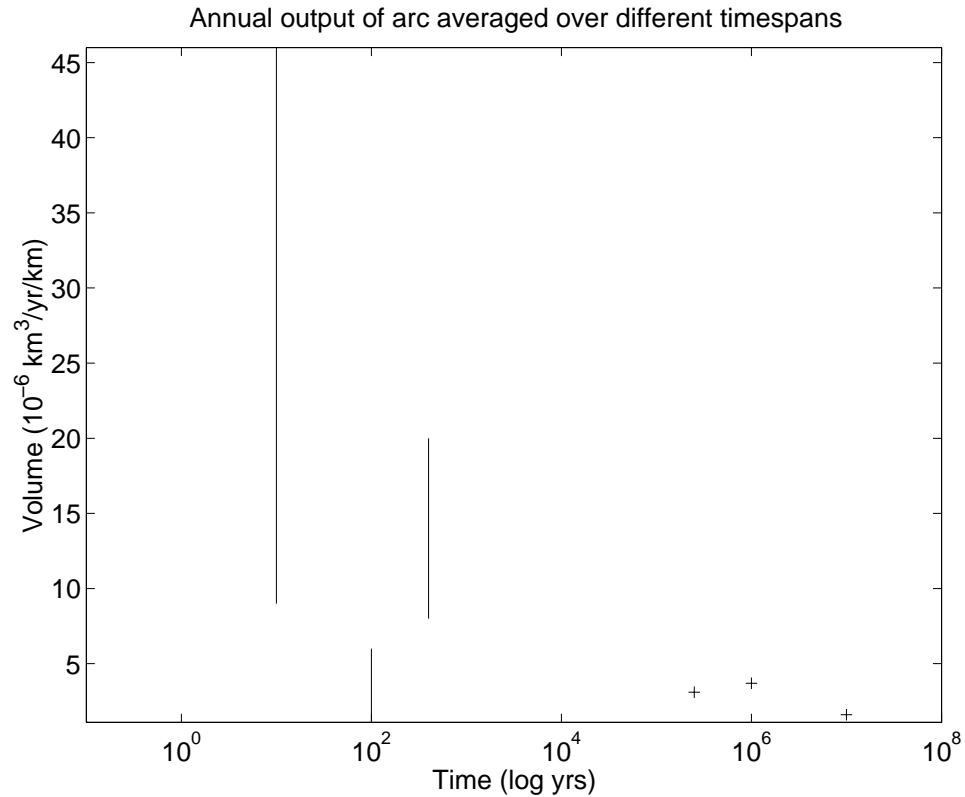


Figure 2.14: Estimates of volcanic output averaged over different timespans (10, 100, 400,  $2.5 \times 10^5$ ,  $10^6$ , and  $10^7$  yr). The three longest timespans are from *Francis and Hawesworth* (1994) who summed the volume of the volcanic edifices with the inferred ages. For the other time periods, we have used the range in estimated erupted products from the Smithsonian database (*Smithsonian Institution*, 2003; *Simkin and Siebert*, 1994), with additional volume constraints for large eruptions: Huaynaputina, 1600 (*Thouret et al.*, 2002; *Adams et al.*, 2001); Sabancaya, 1990 (*Thouret et al.*, 1995); Lascar, 1986 (*Glaze et al.*, 1989) and Lascar, 4/1993 (*Deruelle et al.*, 1996; *Smithsonian Institution*, 1994c). The various estimates are within an order of magnitude, although the fact that the 100 year average is lower than the adjacent values is probably a result of the episodicity of volcanic eruptions, because between the important 1600 Huaynaputina and 4/1993 Lascar eruptions, there were only moderate eruptions.

## 2.5 Conclusions

A principle goal of this survey of volcanic activity was to determine the depths of magma chambers at several volcanic edifices, in order to understand whether magma plumbing is the same at different centers within an arc. Our experiments with different elastic media, the trade-off between source depth and strength, and different source geometries indicate that our observed volcanic deformation could be due to magma activity within a range of depths, but that this range is usually less than 10 km. From north to south, the inferred source depths (below sea level) are: 8-18 km at Hualca Hualca; 12-25 km for Uturuncu; 5-13 km for the Lazufre, and 5-10 km at Cerro Blanco (Table 2.2). As an independent check on source depth, it would be of interest to know the depth of microseismicity in the region of each center of volcanic deformation. For example, a limited array of seismometers near Hualca Hualca found earthquakes at depths between 4 and 7 km below sea level in 1990 (*Lazo et al.*, 1991). It is possible that this seismicity is consistent with our deeper source, that the source depth has increased with time, or that the seismically and/or geodetically inferred depths are inaccurate. It is unclear whether shallow seismicity at Uturuncu detected in April 2003 is related to the magma body (Chapter 1). The maximum source depths at Uturuncu and Hualca Hualca are among the deepest ever determined using geodetic data. Prior to the late 1990's, only calderas had reliable source depths greater than 6 km (Medicine Lake, Yellowstone, and Long Valley, USA; Aira and Sakurajima, Japan, *Dvorak and Dzurisin*, 1997). The deepest sources inferred from deformation observed with geodetic data from other arcs are as follows: 9 km Westdahl, Aleutians (*Lu et al.*, 2000c); 6.5 km South Sister, Cascades (*Wicks et al.*, 2002); 7.9 km Mount Iwate, Japan (*Nishimura et al.*, 2001); 7 km Hengill, Iceland (*Feigl et al.*, 2000); 5 km Cerro Azul, Galapagos (*Amelung et al.*, 2000); 8.5 km Merapi, Indonesia (*Beauducel and Cornet*, 1999); 6-16 km Mt. Etna, Italy, (for discussion of the range of depths, see Chapter 1). The lack of deformation associated with eruptions has also been used to constrain chamber depths, although explanations other than a deep chamber are possible (Chapter 1): > 16.5 km Fogo, Cape Verde (*Amelung and Day*, 2002); > 7 km

Piton de la Fournaise, Reunion (*Sigmundsson et al.*, 1999). The deeper source depths in the central Andes might be related to the thicker crust (50-70 km), in this arc relative to the other arcs.

The cause of deformation at the four volcanoes is ambiguous, although some constraints can be made. Because hydrothermal systems are usually less than 10 km deep, the  $> 16$  km source depth for deformation at Uturuncu suggests a magmatic origin. This source may be related to a region of low seismic velocity and inferred partial melt (*Chmielowski et al.*, 1999), part of the Altiplano-Puna Magmatic Complex (*de Silva*, 1989). The dimensions of the partially molten region are well constrained by several seismic arrays in the area, but the inferred depth and thickness of the magma body are model dependent (and particularly sensitive to how the strong anisotropy above the magma body is modeled, *Leidig and Zandt*, 2003). Plausible depths to the magma body are between 14-17 km below local relief (*Zandt et al.*, 2003). Support for the existence of partial melt in this area also comes from seismic attenuation studies (*Haberland and Rietbrock*, 2001) and electromagnetic experiments (*Schilling et al.*, 1997). Lazufre and Cerro Blanco lie near regions with low seismic velocities, but more than 200 km from the lowest velocities (*Yuan et al.*, 2000; *Zandt et al.*, 2003). As shown in the calculations above, subsidence at Cerro Blanco is not caused by only by conductive cooling or crystallization of a magma body, but is augmented by hydrothermal activity – either release of previously built-up pressure in the hydrothermal system, or the withdrawal of fluids.

Deformation at all four sources is time-dependent, and while these variations in deformation might represent normal intrinsic fluctuations, some of the changes could be related to external processes. The changes in activity at Uturuncu and Lazufre could represent the influence of a  $M_w$  7.1 subduction zone earthquake in 1998. Such remote triggering of deformation in volcanic areas has been observed before, and a variety of mechanism might be involved (e.g., *Barrientos*, 1994; *Johnston et al.*, 1995; *Brodsky*, 2001). Inflation at Hualca Hualca stopped in 1997, perhaps related to a large eruption of nearby Sabancaya volcano in May, 1997, although there is no obvious relation between the rate of deformation and the eruptions of Sabancaya (Chapter 1).

We infer indirect evidence of subsidence between late 1997 and early 1999, to account for the fact that inflation (albeit barely above the detection threshold) seems to be in interferograms spanning 1995-1997, but not in interferograms spanning 1995-2001 (Figure 2.8).

Three of the four centers of deformation found in this survey are offset from the eruptive vent on the volcanic edifice. The offset is model dependent (Table 2.2), but is about: 5 km at Uturuncu, Bolivia; 7-10 km at Lazufre (the smaller value is appropriate if the chamber feeds Cordon del Azufre and the larger number is favored if the chamber feeds Lastarria); and 3-8 km at Hualca Hualca (where the smaller number represents the distance between Hualca Hualca and the chamber and the larger number is the distance to the more active Sabancaya). A horizontal offset between the source of deformation and an eruptive vent is seen in many locations: about 2 km at Mt. Peulik, Alaska (*Lu et al.*, 2002c); 5 km at South Sister, Oregon (*Wicks et al.*, 2002), and Makushin, Alaska (*Lu et al.*, 2002b); and 13 km at Mt. Iwate, Japan (*Nishimura et al.*, 2001). Several eruptions seem to have been fed by magma chambers 5-10 km away from the eruptive center at Novarupta, Alaska in 1912 (*Curtis*, 1968), and at Okmok, Alaska in 1997 (*Lu et al.*, 2000b). The magma chamber near Hualca Hualca might have fed eruptions at nearby Sabancaya, but there is no obvious deflation of the magma chamber associated with the largest eruption spanned by the radar data in May 1997. Recent modeling indicates that a magma chamber offset from the edifice can still feed eruptions on the edifice, because dikes from the distant magma chamber are focused by the local topographic stresses toward the edifice (*Muller et al.*, 2001). However, the reason that the intrusion occurs in a magma chamber offset from the central edifice is unknown – is this a location favored by the local stress field, by the process of melt migration from deeper levels, or is it just random where an intrusion will occur?